



## Article

# Benefits of Combining ALOS/PALSAR-2 and Sentinel-2A Data in the Classification of Land Cover Classes in the Santa Catarina Southern Plateau

Jessica da Silva Costa <sup>1,2</sup>, Veraldo Liesenberg <sup>1</sup>, Marcos Benedito Schimalski <sup>1</sup>, Raquel Valério de Sousa <sup>2</sup>, Leonardo Josué Biffi <sup>2</sup>, Alessandra Rodrigues Gomes <sup>3</sup>, Sílvio Luís Rafaeli Neto <sup>2</sup>, Edson Mitishita <sup>4</sup> and Polyanna da Conceição Bispo <sup>5,\*</sup>

- <sup>1</sup> Department of Forest Engineering, College of Agriculture and Veterinary, Santa Catarina State University (UDESC), Avenida Luiz de Camões 2090, Lages SC 88520-000, Brazil; jessica.costa@edu.udesc.br (J.d.S.C.); veraldo.liesenberg@udesc.br (V.L.); marcos.schimalski@udesc.br (M.B.S.)
  - <sup>2</sup> Department of Environmental and Sanitation Engineering, College of Agriculture and Veterinary, Santa Catarina State University (UDESC), Avenida Luiz de Camões 2090, Lages SC 88520-000, Brazil; raquel.sousa@udesc.br (R.V.d.S.); leonardo.biffi@udesc.br (L.J.B.); silvio.rafaeli@udesc.br (S.L.R.N.)
  - <sup>3</sup> Amazon Regional Center, Brazilian National Institute for Space Research (INPE), Avenida Perimetral 2651, Belem PA 66077-830, Brazil; alessandra.gomes@inpe.br
  - <sup>4</sup> Graduate Program in Geodetic Sciences, Federal University of Paraná (UFPR), Avenida Coronel Francisco Heráclito dos Santos 210, Curitiba PR 81531-990, Brazil; mitishita@ufpr.br
  - <sup>5</sup> Department of Geography, School of Environment, Education and Development, University of Manchester, Oxford Road, Manchester M13 9PL, UK
- \* Correspondence: polyanna.bispo@manchester.ac.uk



**Citation:** Costa, J.d.S.; Liesenberg, V.; Schimalski, M.B.; Sousa, R.V.d.; Biffi, L.J.; Gomes, A.R.; Neto, S.L.R.; Mitishita, E.; Bispo, P.d.C. Benefits of Combining ALOS/PALSAR-2 and Sentinel-2A Data in the Classification of Land Cover Classes in the Santa Catarina Southern Plateau. *Remote Sens.* **2021**, *13*, 229. <https://doi.org/10.3390/rs13020229>

Received: 1 December 2020

Accepted: 5 January 2021

Published: 11 January 2021

**Publisher's Note:** MDPI stays neutral with regard to jurisdictional claims in published maps and institutional affiliations.



**Copyright:** © 2021 by the authors. Licensee MDPI, Basel, Switzerland. This article is an open access article distributed under the terms and conditions of the Creative Commons Attribution (CC BY) license (<https://creativecommons.org/licenses/by/4.0/>).

**Abstract:** The Santa Catarina Southern Plateau is located in Southern Brazil and is a region that has gained considerable attention due to the rapid conversion of the typical landscape of natural grasslands and wetlands into agriculture, reforestation, pasture, and more recently, wind farms. This study's main goal was to characterize the polarimetric attributes of the experimental quad-polarization acquisition mode of the Advanced Land Observing Satellite/Phased Array type L-band Synthetic Aperture Radar (ALOS/PALSAR-2) for mapping seven land cover classes. The polarimetric attributes were evaluated alone and combined with SENTINEL-2A using a supervised classification method based on the Support Vector Machine (SVM) algorithm. The results showed that the intensity backscattering alone reached an overall classification accuracy of 37.48% and a Kappa index of 0.26. Interestingly, the addition of polarimetric features increased to 71.35% and 0.66, respectively. It shows that the use of polarimetric decomposition features was relatively efficient in discriminating land cover classes. SENTINEL-2A data alone performed better and achieved a weighted overall accuracy and Kappa index of 85.56% and 0.82. This increase was also significant for the Z-test. However, the addition of ALOS/PALSAR-2 derived features to SENTINEL-2A slightly improved accuracy and was marginally significant at a 95% confidence level only when all features were considered. Possible implications for that performance are the accumulated precipitation prior to SAR data acquisition, which coincides with the rainy season period. The experimental quad-polarization mode of ALOS/PALSAR-2 shall be evaluated in the near future over different seasonal conditions to confirm results. Alternatively, further studies are then suggested by focusing on additional features derived from SAR data such as texture and interferometric coherence to increase classification accuracy. These measures would be an interesting data source for monitoring specific land cover classes such as the threatened grasslands and wetlands during periods of frequent cloud coverage. Future investigations could also address multitemporal approaches employing either single or multifrequency SAR.

**Keywords:** SAR mapping; data fusion; polarimetric attributes; mapping purpose; supervised classification; classification accuracy; Coxilha Rica; Southern Brazil

## 1. Introduction

Optical orbital sensor systems, such as those in the Landsat series, are generally used in mapping land use and land cover (LULC). However, the frequent cloud cover in tropical regions ends up restricting the acquisition of information based on the exclusive use of these sensors. Nonetheless, the use of a radar system becomes a viable alternative to this limitation due to the ability to collect data in almost all climatic conditions [1–4].

Unlike sensors that record electromagnetic radiation reflected or emitted by objects in the optical range of the electromagnetic spectrum, synthetic aperture radar (SAR) operates in the microwave range. Radars are active sensors; that is, they do not depend on solar energy and can operate day and night with the transmission and reception of electromagnetic radiation in this spectral range. Depending on the selected frequency and the polarization mode used, the information collected can reveal geometric properties of soils and plant canopies [5–7]. Single and double polarization modes are the most common acquisition modes. The full data acquisition mode, with four polarizations, also known as quad-polarization, is still experimental.

Polarimetry records the amplitude and phase information that allows inferring about the geometric and dielectric properties that can be useful in characterizing tropical environments. Techniques for decomposing polarimetric data can reveal backscattering mechanisms that occur during SAR data acquisition. Therefore, they reveal geometrical properties whose information can serve as additional information in land cover mappings reported in different studies [3,8–13].

SAR data has been widely used in land cover mapping initiatives, including the study conducted by Freitas, Sano, Souza [14]. These researchers analyzed ALOS/PALSAR images (L band, HH, HV, and VV polarizations) to discriminate different land cover classes in the middle Taquari region, in the municipality of Corumbá (Mato Grosso do Sul State). The study conducted by Camargo et al. [10] evaluated the use of ALOS/PALSAR-2 images in mapping classes of land use and land cover in the Cerrado biome. More recently, in the study led by Wiederkehr et al. [11,15], who analyzed the potential of attributes derived from intensity backscattering coefficients and target decomposition techniques from the ALOS/PALSAR-2 full polarimetric data for the discrimination of land cover classes in the region of Tapajós National Forest (Eastern Amazon, Brazil).

The biggest problem related to using and exclusively analyzing the SAR images is the complex interpretation inherent to this type of data [16–18]. It is difficult to understand the interaction that effectively occurs between the radiation emitted by the SAR sensor and the target due to the frequent unavailability of reliable data on the dielectric and geometric conditions of the soils and vegetation at the moment the sensor system passes. SAR signals are also dependent on imaging parameters related to wavelength, incidence angle, and polarization mode [18].

Thus, using a single type of sensor (optical or SAR) does not provide enough information about the phenomena and/or objects under study. Optical data is related to the chemical, physical, and biological characteristics of targets. In contrast, SAR data is associated with shape, texture, structure, and dielectric properties. Thus, the combined use of both optical and SAR data can result in improvements in classifying the land cover in complex environments [2,3,19,20]. Such studies were carried out by Pavanelli et al. [3], Souza Mendes et al. [4], Pereira et al. [20], and Liesenberg et al. [21]. All these initiatives were developed to analyze the ability to integrate SAR data with optical data in the classification of the land use and land cover classes in the Amazon biome (Brazil).

Interestingly, almost all of the studies mentioned above are carried out inside the Brazilian Amazon region, where several quad-polarization acquisition modes from ALOS/PALSAR-2 scenes are also available. As a result, studies aiming to use this data in the country's southern region are still incipient, more precisely in the Santa Catarina Southern Plateau. This region is inserted in the "Coxilha Rica" region, which presents the largest remnant area of natural grasslands in Southern Brazil. It consists of shrubby wetlands and preserved araucaria forests remnants of the State of Santa Catarina. It also has a historical and

cultural significance as part of “The Merchants’ Road”, a route used by “tropeiros” in the 18th century to transport cattle from Rio Grande do Sul to Sao Paulo (Southeastern Brazil). This activity was responsible for developing the region’s trade and economy. Still, it is a region with great cloud coverage incidence that hinders mapping initiatives based purely on optical images, highlighting the need to develop studies to carry out mappings of this region’s land cover. Thus, the hypothesis is formulated that the use of microwave data would perform similarly to optical images for land cover mapping initiatives. However, their combined use allows even better land cover classes and benefits land cover mapping initiatives.

In this context, the objective of this study is to extract polarimetric attributes from data acquired in the experimental “full” polarimetric mode of ALOS/PALSAR-2 and its potential and combined with optical data from the SENTINEL-2A sensor for mapping purposes at higher southern latitudes in Southern Brazil.

## 2. Materials and Methods

### 2.1. Study Area Description

The study area covers the Santa Catarina Southern Plateau, and it is located at longitude  $50^{\circ}7'36.34''$  W and latitude  $27^{\circ}54'12.76''$  S, covering a territorial area of approximately  $3000\text{ km}^2$  (Figure 1). It is a region that has gained considerable attention due to the rapid conversion of the typical landscape of natural grasslands and wetlands into agriculture, planted forests, pasture, and, more recently, wind farms for energy production.

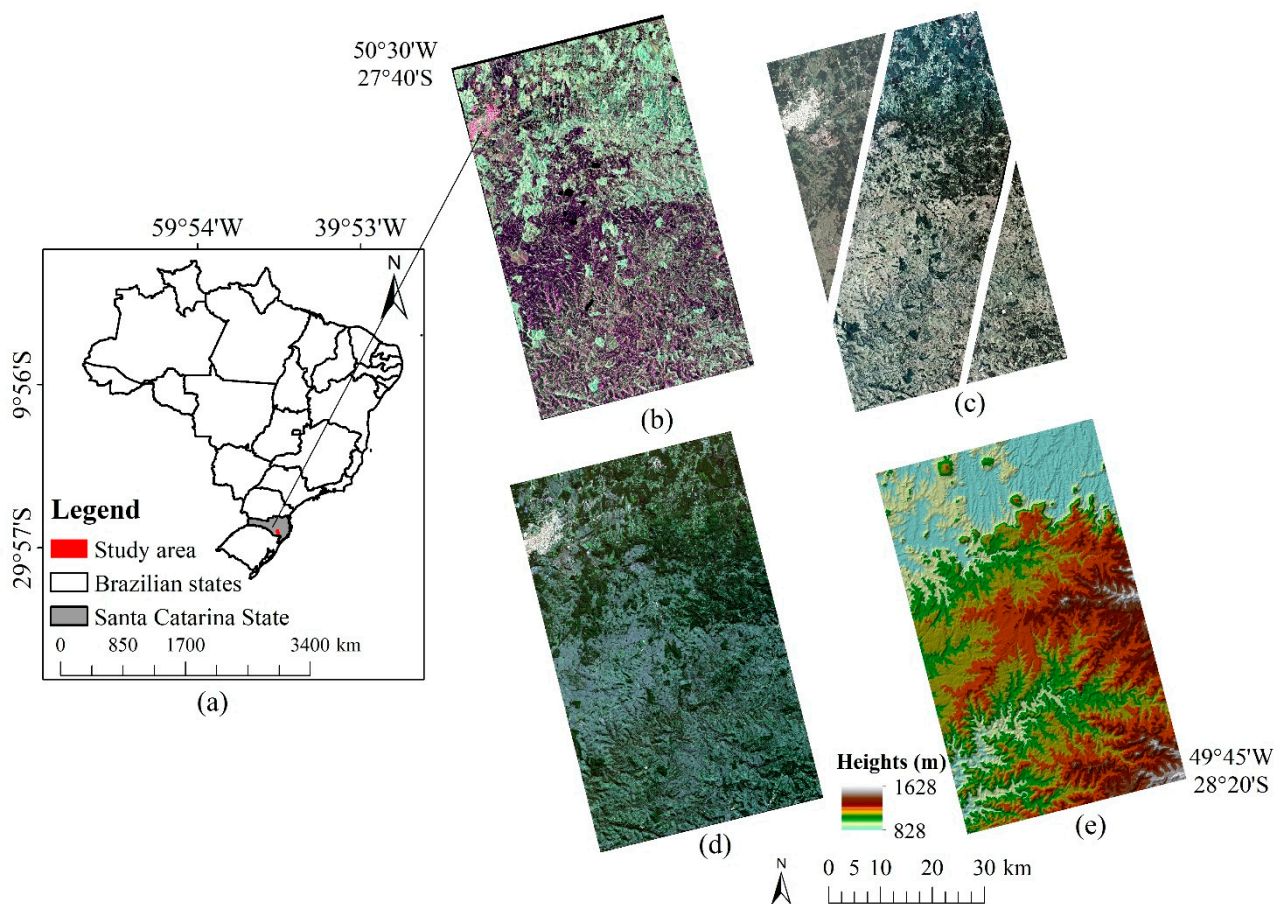


**Figure 1.** Location of the study area within the national context (a). The letters show the ALOS/PALSAR-2 data (R:HH, G:HV, B:VV) (b), PlanetScope images (R:3, G:2, B:1) (c), SENTINEL-2A image (R:4, G:3, B:2) (d) and the SRTM digital elevation model (e) for the study area.

The study site is also partly located in “Coxilha Rica” and is part of the southern portion of the municipality of Lages, corresponding to approximately 43% of the municipality’s area, comprising a large undulating plateau of native grasslands with typical wetlands and with remnants of the uneven-aged mixed ombrophilous forests (MOF). MOF is one of the Atlantic Forest Biome’s most characteristic formations in which *Araucaria angustifolia* (Bertol.) Kuntze is the dominant tree species. Still, the region is characterized by the development of livestock activities, such as extensive cattle farming practiced in native grasslands with several grass species [22,23]. The region has an average altitude of 740 m above sea level and a climate classified as Cfb (subtropical temperate), with an average temperature of 16 °C [24]. According to the mapping of Brazil’s vegetation, produced by IBGE [25] at a scale of 1:5,000,000, the study region has a natural vegetation cover of MOF (Araucaria Forest) and Native grasslands (Southern Brazilian Grasslands). Landscape perspectives of the study area and containing different land cover classes are shown in Figure A1 (Appendix A).

## 2.2. Remote Sensing Datasets

This study used radar data from the Advanced Land Observing Satellite (ALOS-2) of the Phased-Array L-Band Synthetic Aperture Radar (PALSAR-2) sensor developed by the Japanese Space Agency (Japan Aerospace Exploration Agency—JAXA) (Table 1a; Figure 1b). To interpret the existing features and sample collection, images of the constellation PlanetScope acquired on the same date and covering more than 95% of the study area (Table 1b; Figure 1c) were used. Both PALSAR-2 and PlanetScope were acquired on February 23, 2018. A clear sky image from the SENTINEL-2A sensor (Table 1c; Figure 1d) with an imaging date of June 09, 2018, was also used. It shows few changes in land cover compared to the image of the same sensor of February 23, 2018, thus facilitating its visual interpretation and selecting both training and validation datasets for the statistical assessment and classification procedures. The Digital Elevation Model (DEM) from the Shuttle Radar Topography Mission (SRTM) is shown in Figure 1e.

**Table 1.** Characteristics of ALOS/PALSAR-2 (a), PlanetScope (b) e SENTINEL-2A (c) sensors.

(a) ALOS/PALSAR-2	
Acquisition Date	02/23/2018 (experimental mode)
Wavelength	(approx. 23 cm) L band
Operating mode	Full Polarimetric (PLR)
Polarizations	Quad-pol (HH, VV, HV, VH)
Orbit	Ascending
Pixel spacing	2.79 m (range) × 2.86 m (azimuth)
Angle of incidence	33.2°
Final spatial resolution	20 m in range × 20 m in azimuth
Number of rows and columns	25,960 × 8816
(b) PlanetScope	
Acquisition Date	02/23/2018
Central wavelength (nm)	VIS: 485, 545, 630 nm. Near-infrared(NIR): 820 nm
Spatial resolution (m)	~3.0
Radiometric resolution (bits)	12
Temporal resolution	Daily
(c) SENTINEL-2A	
Acquisition Date	06/09/2018
Central Wavelength (nm)/Spatial Resolution	10 m: VIS (B2: 492.4, B3: 559.8, B4: 664.6), NIR (B8: 832.8) 20 m: red-edge (B5: 704.1, B6: 740.5, B7: 782.8), NIR (B8A: 864.7), shortwave-infrared (SWIR) (B11: 1613.7, B12: 2202.4)
Radiometric resolution (bits)	12
Temporal resolution	10 days

It is noteworthy that in the seven days preceding the acquisition dates of the ALOS/PALSAR-2 and SENTINEL-2A images, 14.30 mm and 21.5 mm of accumulated precipitation were recorded, according to the rain data recorded in the Coxilha Rica pluviometric station (code 2850004) [26]. The characteristics of the aforementioned sensors are shown in Table 1, respectively.

### 2.3. Image Processing

In this work, several processing steps were performed, such as the extraction of polarimetric attributes, the analysis of the selected land cover classes' spectral characteristics, and the classification outcomes of different data input models. All the steps are shown in Figure 2 and are further detailed in the forthcoming subsections.

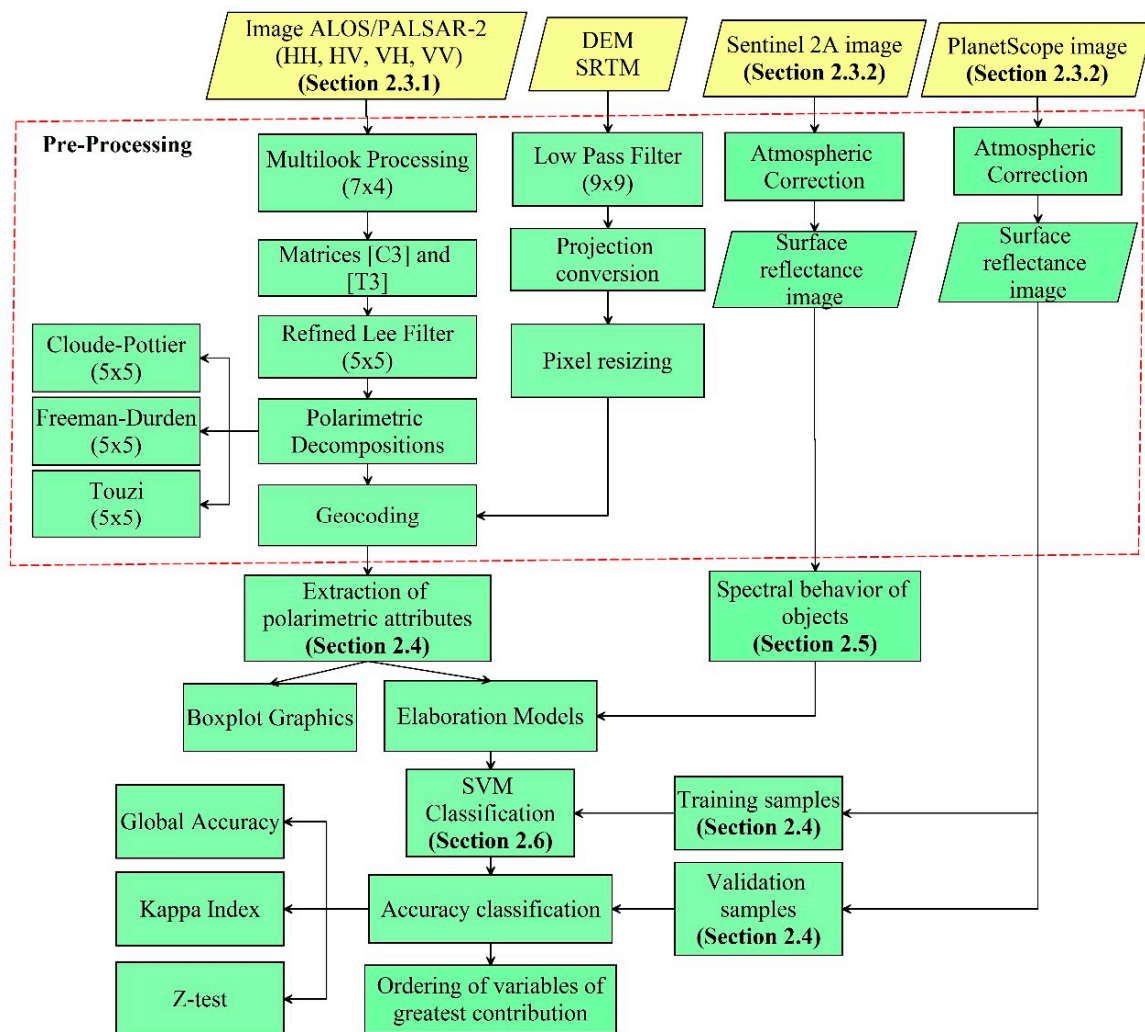


Figure 2. Methodological flowchart of main data processing steps in this study.

#### 2.3.1. ALOS/PALSAR-2 Data Processing

The processing steps of the ALOS/PALSAR-2 full experimental images, acquired at the slant range processing level (level 1.1), included: (1) multi-look processing to obtain data in resolution elements and compatibility with the other stages; (2) application of the filter to minimize the speckle effect; (3) calculation of polarimetric decompositions; and (4) geocoding for orthorectification of the data and insert cartographic information.

From the single look complex (SLC) HH, HV, VV, and VH polarization images, the elements of the scattering matrix [S] were calculated to perform the calculation of the

covariance [C] and coherence [T] matrices [27,28]. In this step, the images were processed in multi-look mode, using seven looks in the range direction and four looks in the azimuth direction. The images' resolution elements of  $2.79 \text{ m} \times 2.86 \text{ m}$  (range  $\times$  azimuth) were resampled in pixels of approximately  $20 \times 20 \text{ m}$  (range  $\times$  azimuth). This procedure is justified to make both SAR and SENTINEL-2A data compatible. In this way, ground range images were generated for the four polarizations analyzed.

The Refined Lee polarimetric filter was applied to matrices [C] and [T] with a  $5 \times 5$  pixel size window, preserving the edges between objects and at the same time smoothing the speckle effect in homogeneous regions [29]. The window size selection was based on both visual interpretation and the speckle suppression index [30]. Thus, this polarimetric filter with this window size was also chosen because it presents good results, according to the reported studies by Mendes et al. [4] when working on the transitional area between Savanna and the Amazon forest, and Mishra et al. [31] by investigating a complex rural and urban area environment in India. After, the Freeman-Durden polarimetric decomposition was calculated from the matrix [C]. The Cloude-Pottier and Touzi polarimetric decompositions were then computed using matrix [T] [8]. In the three decompositions, a  $5 \times 5$  pixel spatial average window was used. These steps were performed using the computer application PolSARpro 6.0<sup>®</sup> [32].

The subsequent processing consisted of performing Range-Doppler terrain correction to transform the slant range images into ground range and geocoding them. In this way, the DEM from the SRTM was selected. Then the spatial frequency filtering was applied to the digital model, using the  $9 \times 9$  low-pass convolution filter. This filter is responsible for emphasizing the low frequencies of the image at the expense of reducing the high frequencies, being a smoothing filter for attenuating the edges' regions and fine details, such as noise, corresponding to the high-frequency components [33]. The conversion of the geographic coordinate system to the Universal Transverse Mercator (UTM) plane coordinate system of the World Geodetic System 1984 (WGS-84) datum from the DEM mentioned above was carried out and scaled to  $20 \times 20 \text{ m}$ . It was then used as auxiliary information coupled with 12 ground control points (GPC) distributed over certain geomorphological features captured from high spatial resolution images. The main objective was to geocode ALOS/PALSAR-2 data and maintaining compatibility with other data sources. A cross-check of the spatial agreement among datasets was then performed using the geocoded ALOS/PALSAR-2 with the two other optical data sources (SENTINEL-2A and PlanetScope). Such evaluation was conducted between datasets using some artificial structures such as roads and geomorphological features such as water streams and elevations.

### 2.3.2. SENTINEL-2A and PlanetScope Processing Steps

In the SENTINEL-2A image processing stage, atmospheric correction of the images was performed to obtain reflectance data at the bottom of the atmosphere (BOA). The image at level 1C contains reflectance data calculated at the top of the atmosphere (TOA). The spectral images were then converted from digital numbers (DN) into TOA reflectance by dividing by the 10,000-scale factor. Subsequently, the atmospheric correction was performed using the Sen2Cor algorithm [34]. Then, all spectral bands were resampled to the spatial resolution of 20 m to better fit with the ALOS/PALSAR-2 data.

PlanetScope image was used to support the visual analysis of the ALOS/PALSAR-2 data and aid in the collection of both training and validation datasets. The PlanetScope image was converted from digital numbers (DN) into TOA reflectance. The image was already orthorectified and referred to the UTM cartographic projection. The atmospheric effect was minimized using the Fast Line-of-sight Atmospheric Analysis of Spectral Hypercubes (FLAASH) algorithm. The visual analysis showed that the displacement among datasets was imperceptible, and, therefore, no co-registration through manual operation to prevent misleading of subsequent analysis was necessary.

#### 2.4. Selection of the Training and Validation Datasets and the Extraction of Polarimetric Attributes

The SAR features' discrimination potential, such as intensity backscattering coefficients and polarimetric decompositions, presented in Table 2, was analyzed for seven major land cover classes. Table 3 shows a description of these land cover classes and their visual aspect in each remote sensing dataset.

A total of 600 pixels were selected for each land cover class over the ALOS/PALSAR-2 with the aid of the PlanetScope image acquired on the same date. Special attention was given to the spatial distribution of these points to avoid autocorrelation. The dataset was then divided using the random criteria into two parts, i.e., 496 pixels for training and 104 pixels for validation. Since all images were well registered to each other, the pixels have approximately similar locations in each dataset for each land cover class.

The validation dataset was used to evaluate the potential for discrimination through visual analysis of boxplot graphics, generated in the computer application RStudio® [35], using non-parametric descriptive statistics, containing minimum, maximum, first and third quartile, median, and outliers. The precipitation data for February 2018, from the COXILHA RICA rain station (code 2850004) located in Lages municipality, provided by the National Water Agency [26], were used to understand the targets' polarimetric responses.

#### 2.5. Spectral Characterization of the Selected Land Use Classes Using SENTINEL-2A Image

The spectral profile of the seven land cover classes analyzed in this study (Figure 3) was obtained from the surface reflectance of ten spectral bands of the SENTINEL-2A sensor (Table 1c). For this, the corresponding surface reflectance values for each spectral band were collected and averaged from the validation dataset (104 pixels) extracted with the aid of PlanetScope images for each land cover class.

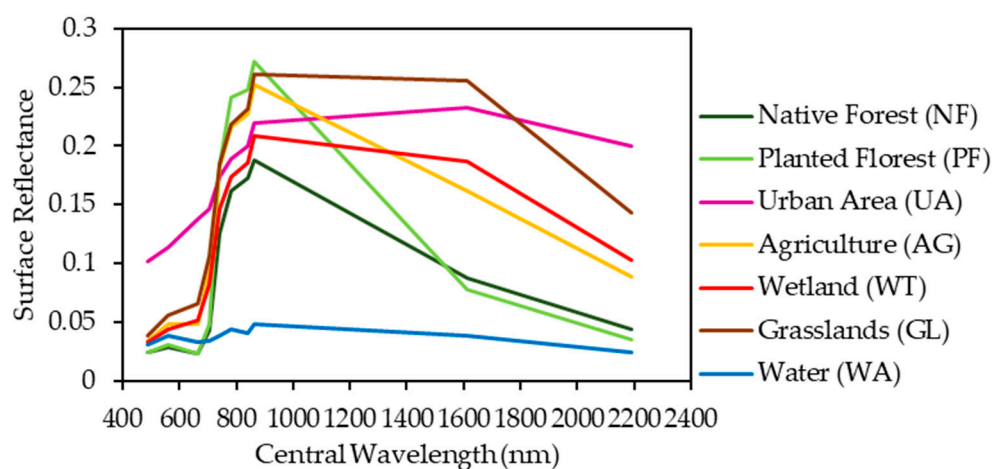


Figure 3. Spectral profile of the seven land cover classes selected considering the SENTINEL-2A image of 9 June 2018.

Table 2. Polarimetric attributes derived from backscattering and polarimetric decompositions.

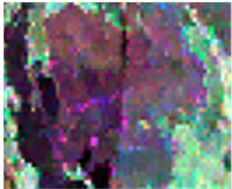
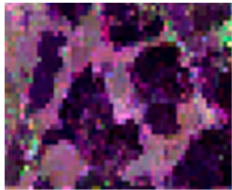
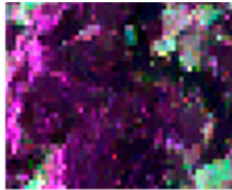
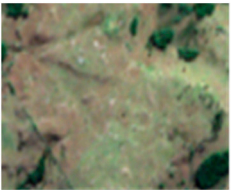
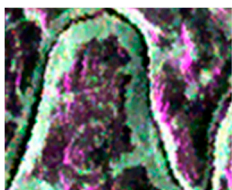
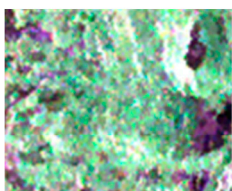
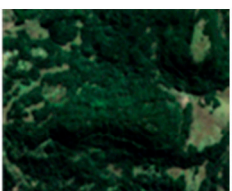
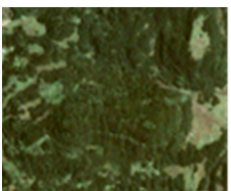
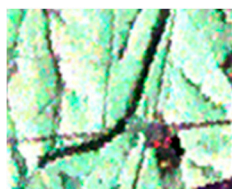
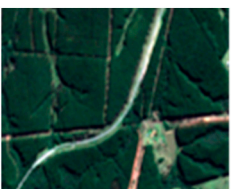
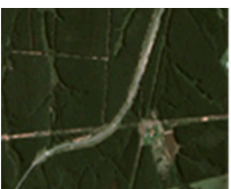
Extracted Attributes	Equation	Description	References
Backscatter coefficient ( $\sigma_{HH}^0, \sigma_{HV}^0, \sigma_{VH}^0, \sigma_{VV}^0$ ) <sup>1</sup>	$\sigma_{ij}^0 = 10 \frac{\sigma_{ij}^0(\text{dB})}{10}$ , where $\sigma_{ij}^0(\text{dB}) = 10 \log_{10} (I^2 + Q^2) + Fc - A$	Indicates the orientation of the forest components.	[36,37]
Relation of Co-Polarization	$Rco = \frac{\sigma_{VV}^0}{\sigma_{HH}^0}$	Highlights different vertical and horizontal orientations derived from the structural aspects of vegetation.	[36]

Table 2. Cont.

Extracted Attributes	Equation	Description	References
Cross Polarization Ratio	$R_{cross} = \frac{\sigma_{HV}^0}{\sigma_{HH}^0}$	Sensitive to the volumetric dispersion of the forest to support classification and reduce topographic effects in backscattering.	[36]
Radar Forest Degradation Index	$RFDI = \frac{\sigma_{HH}^0 - \sigma_{HV}^0}{\sigma_{HH}^0 + \sigma_{HV}^0}$	Ratio designed to assess the strength of the double-bounce mechanism, which is useful for differentiating vegetation.	[38,39]
Phase Difference <sup>2</sup>	$\Delta_{\varphi HH-VV} = \arg(S_{HH}S_{VV}^*)$ $\Delta_{\varphi HH-HV} = \arg(S_{HH}S_{HV}^*)$ $\Delta_{\varphi HV-VV} = \arg(S_{HV}S_{VV}^*)$	Indication of the structure and quantity of biomass	[36]
Entropy	$H = - \sum_{i=1}^3 p_i \log_3(p_i);$ $p_i = \frac{\lambda_i}{\sum_{j=1}^3 \lambda_j}$	Related to the complexity of the forest structure. The most complex and diversified forest has high H, low A, and close to 45°.	[40]
Anisotropy	$A = \frac{\lambda_2 - \lambda_3}{\lambda_2 + \lambda_3}$		
Alpha Angle	$\alpha = \sum_{i=1}^3 p_i \alpha_i$		
Contribution of volume dispersion	$P_v = \frac{8f_v}{3}$	Proportion of volumetric backscatter associated with the forest structure and biomass content.	[27]
Double-bounce dispersion	$P_d = f_d(1 +  \alpha ^2)$	Indication of canopy opening, density, and number of trees (trunks).	
Surface dispersion	$P_s = f_s(1 +  \beta ^2)$	Related to the canopy opening.	
Magnitude of type of Scattering ( $\alpha_s$ )		The magnitude is negatively correlated with biomass, with the tendency to single-bounce and various types of scattering.	[41]
Phase of Scattering ( $\phi_{\alpha_s}$ )		Essential for an unambiguous description of the dispersion of the forest mechanism.	
Orientation Angle ( $\Psi$ )		Compensate for the fluctuating influence of randomly oriented forest dispersal components and the slope of the land on scatters.	
Helicity ( $\tau_m$ )		Expresses the symmetry of forest dispersion, having an inverse correlation with biomass.	

<sup>1</sup> Fc = calibration factor (−83); A = conversion factor (32). <sup>2</sup> arg, S, \* and () denote argument function, complex dispersion amplitude, complex conjugate, and spatial mean, respectively.

**Table 3.** Description of the seven major land cover classes with detail to specific subsets encompassing the seven major land use classes for the three selected remote sensing sensors.

Classes	Description	ALOS/PALSAR-2	SENTINEL-2A	PlanetScope
		R <sub>HH</sub> G <sub>HV</sub> B <sub>VV</sub>	R4G3B2	R3G2B1
Agriculture (AG)	Includes all cultivated land types (soybean, corn, beans, etc).			
Wetland (WT)	Fragmented wet areas with floating or submerged vegetation.			
Grasslands (GL)	Shrubby stratum, sparsely distributed on a grassy-woody carpet used for cattle ranching.			
Water (WA)	It includes rivers, small streams, canals, natural lakes, artificial reservoirs, among others.			
Native Forest (NF)	Vegetation areas covered by native forest and dominated with Araucaria trees.			
Planted Forest (PF)	Vegetation areas covered by planted forest ( <i>Pinus</i> sp. and <i>Eucalyptus</i> sp.).			
Urban Area (UA)	Intensive use areas, structured by buildings and road system.			

## 2.6. Classification Evaluation based on Different Data Input Models

Nine data input models were established from both the ALOS/PALSAR-2 and SENTINEL-2A (Table 4) in the classification scheme. To perform the classification, 496 and 104 pixels were collected and used as training and validation samples for each class, respectively.

**Table 4.** Combinations of nine different data input models.

Model	Data Input	Feature <sup>1</sup>	Number of features
M1	SAR	HH, HV, VH, VV	4
M2	SAR	M1 + (H, A, $\alpha$ )	7
M3	SAR	M2 + (Pv, Pd, Ps)	10
M4	SAR	M3 + ( $\alpha_s$ , $\phi_{\alpha s}$ , $\Psi$ , $\tau_m$ )	14
M5	SAR	M4 + (Rco, Rcross, RFDI)	17
M6	SAR	M5 + ( $\Delta(HH - VV)$ , $\Delta(HH - HV)$ , $\Delta(HV - VV)$ )	20
M7	Optical	B02, B03, B04, B05, B06, B07, B08, B11, B12, B8A	10
M8	Optical/SAR	M7 + M1	14
M9	Optical/SAR	M7 + M6	30

<sup>1</sup> HH, HV, VH, VV = Backscatter coefficient; H = Entropy; A = Anisotropy;  $\alpha$  = Alpha Angle; Pv = Contribution of volume dispersion; Pd = Double-bounce dispersion contribution; Ps = Contribution of surface dispersion;  $\alpha_s$  = Magnitude of the type of scattering;  $\phi_{\alpha s}$  = Phase of the scattering type;  $\Psi$  = Orientation angle;  $\tau_m$  = Helicity; Rco = Co-Polarization Ratio; Rcross = Cross Polarization Ratio; RFDI = *Radar Forest Degradation Index*;  $\Delta(HH - VV)$ ,  $\Delta(HH - HV)$ ,  $\Delta(HV - VV)$  = Phase difference; and Bi = spectral bands of the SENTINEL-2A sensor described in Table 2.

The Support Vector Machine (SVM) classification algorithm was used in this classification step. It was chosen because it presents better classification results, as shown in the works by Camargo et al. [10], Mishra et al. [31], Attarchi and Gloaguen [42] and Üstüner et al. [43]. SVM is a non-parametric technique based on statistical learning theory. SVM's main objective is to build an ideal separation hyperplane between linearly separable classes within a multidimensional resource space. It was designed to maximize the margin between the ideal separation hyperplane and the closest training samples called support vectors [31,44]. To perform the classification, the radial base core function (RBF) was used. This function has two parameters, cost (C) and gamma (g). A high C value can over-adjust the model to the data while setting the parameter g will influence the way the hyperplane is separated [45]. Parameters (C) and (g) were adjusted by the computer application EnMAPToolBox<sup>®</sup> [46], with search space values between 0.01 and 1000.

Subsequently, the classification accuracy of the different established data input models was analyzed by calculating from the error matrix, the weighted overall classification accuracy, the Kappa index, and the Z-test at 95% confidence level with a critical value of 1.96. After, both user's accuracy (or commission error) and producer's accuracy (or omission error) were obtained for each land cover class and data input model. These metrics were calculated considering each land cover class's weight based on their representativeness in area over the landscape [47,48]. Following the concepts of Olofsson et al. [47,48], the standard error of the weighted overall classification accuracy and Kappa index and both upper and lower limit scores at a 95% confidence interval were then determined for each data input model to support discussion.

Finally, the features used to classify the nine different models were ordered according to their contribution to each classification. Although this step also utilized the overall classification accuracy criteria, it was realized without considering the weight for the individual land cover classes mentioned previously. For this specific step, the direct selection method was used and provided insights for the best features that contribute to the final classification. This method starts with an empty set, and the SVM is applied to each single feature within each data input model (Table 4). The feature corresponding to the SVM with the best individual performance is then selected. The SVM is then

applied to each pair of features, consisting of the best-performing one previously and an additional next one. Once again, the pair of features corresponding to the best performing SVM is then selected. This step is repeated until all features are selected. It results in a classificatory list of features with corresponding performances. The computational application ENMAPToolBox<sup>®</sup> [46] was used to calculate the classification accuracy and to perform the ordering of the features used to classify the nine data input models according to their importance for each classification.

### 3. Results and Discussions

#### 3.1. Spectral Behavior of Land Cover Classes of SENTINEL-2A Image

Figure 3 shows the spectral behavior of the seven land cover classes analyzed in this study (Table 3), considering the spectral bands from the SENTINEL-2A satellite (Table 1). The results showed that in the visible region (490–665 nm), the surface reflectance values are very close for the selected classes, except for the UA class, indicating that there is a difficulty in distinguishing the remaining classes in these wavelengths, mainly in the blue band (490 nm). UA showed a distinguished spectral response from all remaining classes due to a complex set of specific environments in the study area, ranging from residences to buildings. Even some residential areas have parcels with small orchards. The infrastructure consists of bare soil patches to roads with asphalt and paving stone. All these elements contribute to a stronger reflectance in both visible and SWIR spectral regions [49].

It is possible to observe in Figure 3 that in the wavelengths related to the red-edge (705, 740, 783 nm) and the near-infrared (842 nm), there was an increase in the reflectance curve for the classes NF, PF, UA, AG, WA, and GL, and with red-edge-4 (865 nm) obtaining the highest reflectance value for these classes. Still, there was greater discrimination between the analyzed classes, except between the AG and GL classes that present surface reflectance values very close to each other, presenting a difficult distinction between these two similar classes. The WA class showed the lowest reflectance values, and it was easily distinguished from the other classes between the range of 705 to 2190 nm. The spectral profiles show that the surface reflectance for the spectral interval corresponding to the SWIR (1610 and 2190 nm) decreased for the classes NF, PF, WT, GL, and AG due to the presence of water in the leaves. It can still be seen that there is a difficulty in discriminating between classes NF and PF and between classes WT and AG. In general, the spectral behavior of the land use classes (Figure 3) is in agreement with that presented in the studies conducted by Herold et al. [49], Radoux et al. [50], Sothe et al. [51], Prieto-Amparan et al. [52] and Osgouei et al. [53].

From Figure 4a,b, it is possible to observe by the scatterplots between the surface reflectance values of the spectral bands of the red (665 nm) and the edge of the red (705 nm) with the near-infrared (NIR) band (842 nm), respectively, that both WA and UA present greater discrimination between the analyzed classes. In general, these three spectral bands seem to be more optimal for land cover mapping. The dispersion between the surface reflectance values of the Red-Edge bands 2, 3, and 4 with the NIR band shows greater discrimination of the WA class from the other land cover classes (Figure 4c–e).

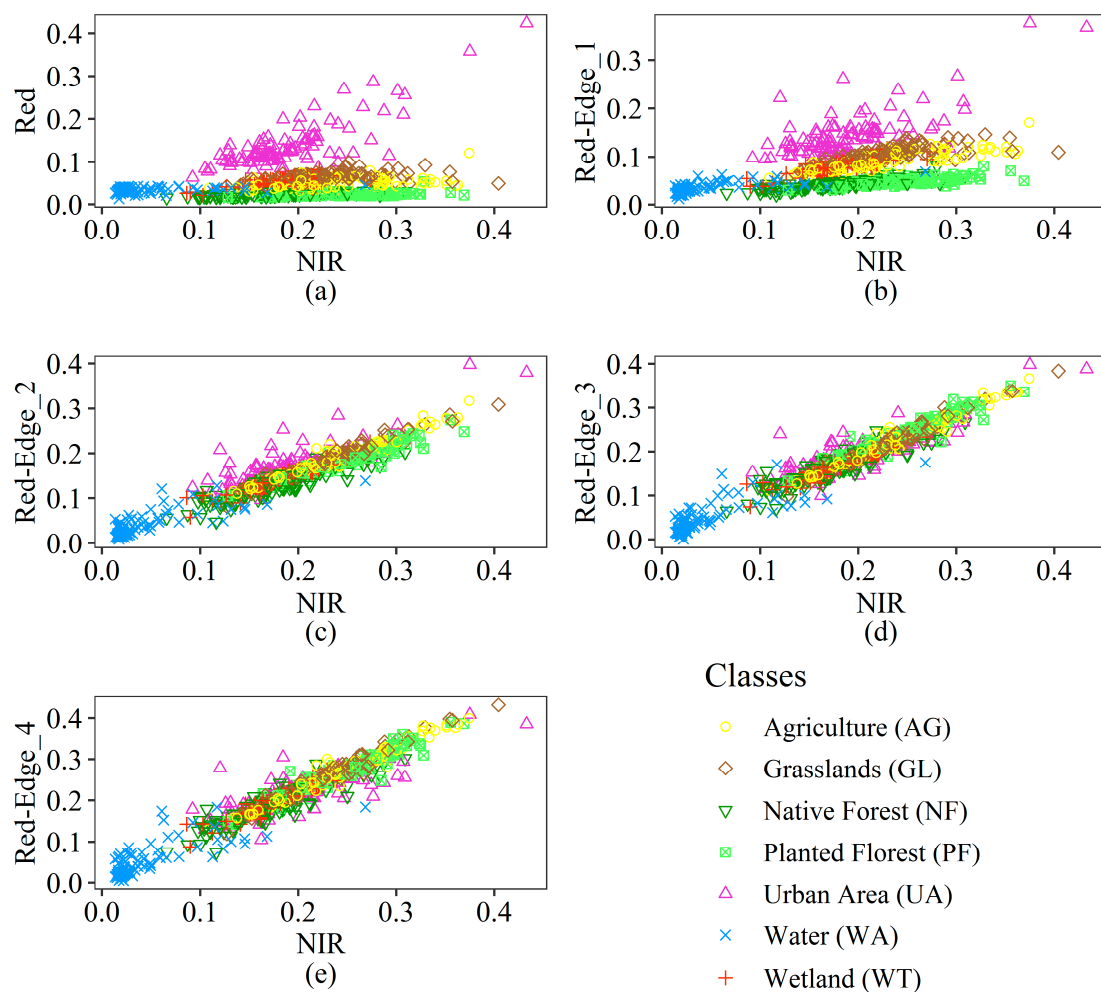


**Figure 4.** Scatterplot for land cover classes between the surface reflectance values of the bands (Red) and NIR (a), Red-Edge-1 and NIR (b), Red-Edge-2 and NIR (c), Red-Edge-3 and NIR (d) and Red-Edge-4 and NIR (e). The description of the spectral bands is in Table 1c.

### 3.2. Discriminatory Analysis of Polarimetric Attributes from SAR Data

In Figure 5, it is possible to observe that the intensity backscattering coefficient values ( $\sigma^0$ ) in both the HH and VV polarizations were quite similar to each other. There is a small tendency for the HH polarization to present higher  $\sigma^0_{HH}$  values, which may be related to the predominance of oriented branches horizontally in the canopy [14,54]. However, the HV cross-polarization values were lower compared to the parallel polarizations. In HV polarization, volumetric backscattering predominates. The multiple backscatters that occur inside the canopy cause a reduction in the radar signal that returns to the antenna [36]. Still, it can be seen that the PF, NF, and UA classes have higher values of backscatter coefficient, classes AG and WT with average backscatter values, and classes WT and GL with low-intensity backscattering coefficient values.

The classes of forest cover NF and PF (Figure 6) present high average values of  $\sigma^0$  for the four polarizations. In these classes, the presence of many leaves, branches, and trunks stands out, with little soil exposure. The denser green biomass and the higher soil moisture are mainly responsible for relatively higher values of  $\sigma^0$  [14,55]. The accumulated precipitation one-week prior SAR data acquisition was 14.3mm. It increased to 64.40 mm when considering two weeks prior SAR data, which undoubtedly contributed to increasing the land cover classes' dielectric constant. The accumulated precipitation is also equivalent to the historical average precipitation for February month. As the mean values for the

NF and PF classes were high for all polarizations, it can be concluded that the larger the vegetation structure, the greater the intensity backscattering coefficients, regardless of the type of polarization [14]. Thus, the HH, HV, VH, and VV polarizations have a high potential for discrimination of the NF and PF classes for the study area.

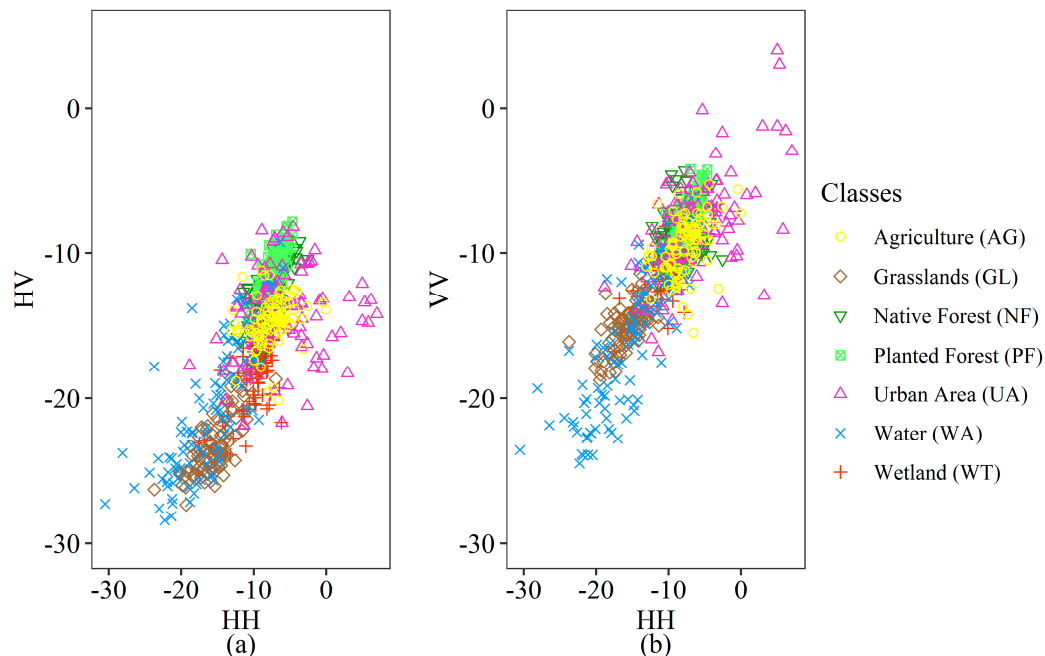


**Figure 5.** Intensity backscattering coefficients between the polarizations HH vs. HV (a) and HH vs. VV (b).

The PF class has a smooth and homogeneous texture and a well-defined geometric shape. Most of its total biomass comes from vertical and rectilinear trunks and branches, which causes a strong reflection in the radar signals [56]. PF intensity backscattering values presented average values of  $-7.350$  dB,  $-11.014$  dB,  $-11.260$  dB, and  $-7.462$  dB for the HH, HV, VH, and VV polarizations, respectively. These values were slightly higher than those obtained for NF what helps discriminating this specific class.

The WT class (Figure 6) presented the following average values of  $-9.550$  dB,  $-17.700$  dB,  $-17.747$  dB,  $-10.500$  dB for the HH, HV, VH, and VV polarizations, respectively. This class has a lower layer stratum of leaves, and these areas are periodically flooded. Due to this low density of green biomass, the  $\sigma^0$  values associated with this class are low compared to the two classes mentioned previously.

In the crossed polarizations, the GL class (Figure 6) presented the lowest mean values of  $\sigma^0$   $-23.053$  dB and  $-23.256$  dB for HV and VH, respectively. This class has a predominantly regular surface, with the presence or absence of shrubs, depending on the management practices applied over these areas. It showed low biomass levels and low soil moisture, associating this class with lower values of  $\sigma^0$  [14].

As for the HH and VV polarizations, the lowest mean values of  $\sigma^0_{HH}$  and  $\sigma^0_{VV}$  obtained were for class WA (Figure 6) with  $-15.752$  dB and  $-16.299$  dB, respectively. The low values on WA are explained by the predominance of specular reflection of incident radiation. In fact, WA is identified on radar images because of their low amplitude values and smooth texture [36]. Thus, obtaining a great discriminatory potential of this class in these polarizations.

The UA class (Figure 6) presented relatively high-intensity backscattering values for the polarizations, standing out in the HH polarization, obtaining the highest value of  $\sigma^0_{HH}$  ( $-6.227$  dB) compared to the other classes. The high values over urban areas are due to the predominance of corner reflections associated with artificial structures such as buildings and residences [18].

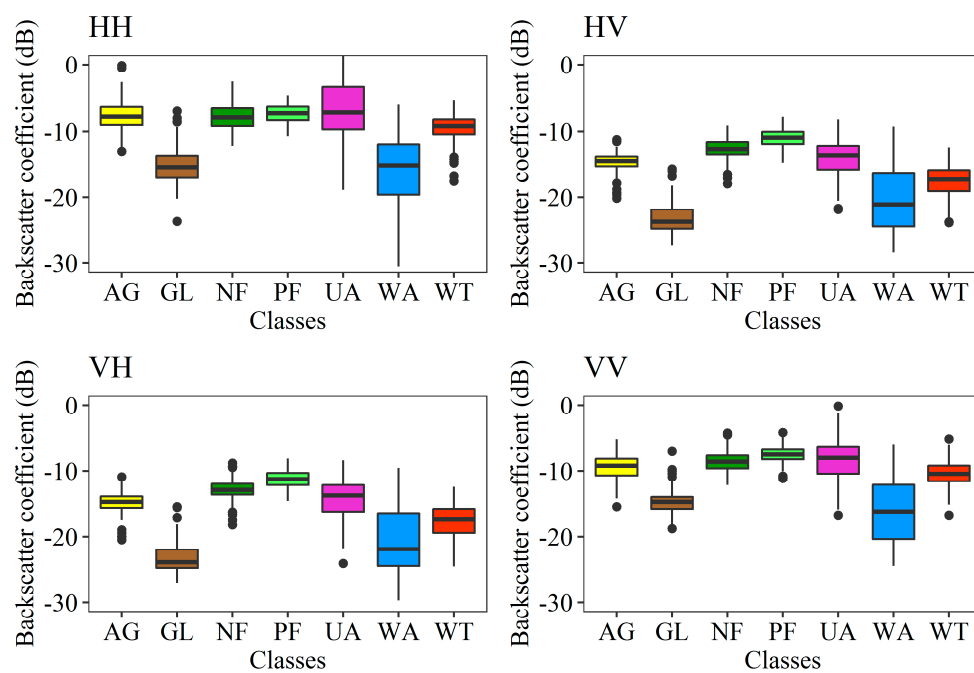


**Figure 6.** Backscatter coefficient (dB) of land cover classes in HH, HV, VH, and VV polarizations. The description of the land cover classes is given in Table 3.

The AG class (Figure 6) showed high-intensity backscattering values, with average values of  $-7.678$  dB,  $-14.708$  dB,  $-14.909$  dB, and  $-9.438$  dB for HH, HV, VH, and VV, respectively. Agriculture areas, depending on the type of existing crop, have a planting dynamic that varies over time. When the analyzed images of the study region were collected, the agricultural area showed well-structured characteristics, thus obtaining high-intensity backscattering values [57].

It is worth noting that the effects of moisture caused by accumulated precipitation can alter intensity backscattering significantly. Unfortunately, there was only a single scene acquired at the quad-polarization mode in the study area. In the SAR data, the ability to capture moisture may vary according to the frequency used. At lower frequencies, such as the L-band, the scattered signal interacts predominantly with branches, trunks, and the soil surface. Before SAR data acquisition, precipitation events increase canopies' moisture content and their components (for example, leaves, branches, trunks, and the soil surface). Thus, the dielectric constant increases and affects the information of the volumetric scattering mechanism. With the increase in moisture, there is less penetration of the canopy incident energy, therefore a greater signal return [21,58]. The accumulated precipitation value recorded, considering the seven days before acquiring the ALOS/PALSAR-2 image was  $14.30$  mm [26], influencing the intensity backscattering values of the land cover classes registered for this image. Therefore, more studies are recommended taking into account quad-polarization scenes in different seasonal conditions such as the dry season. Interestingly, the acquisition of experimental quad-polarization mode occurs only during the first months of each year what coincides with the rainy season [21].

In Figure 7a, it can be seen that the Co-Polarization Ratio (Rco) attribute, extracted from the backscatter coefficients, presented a higher mean value for the GL class (1.178), obtaining a greater contribution from the VV polarization and showing a surface dominant scattering [36]. However, the other classes' averages for the Rco attribute show a small difference between them, indicating a lower capacity of this attribute to differentiate these cover classes.

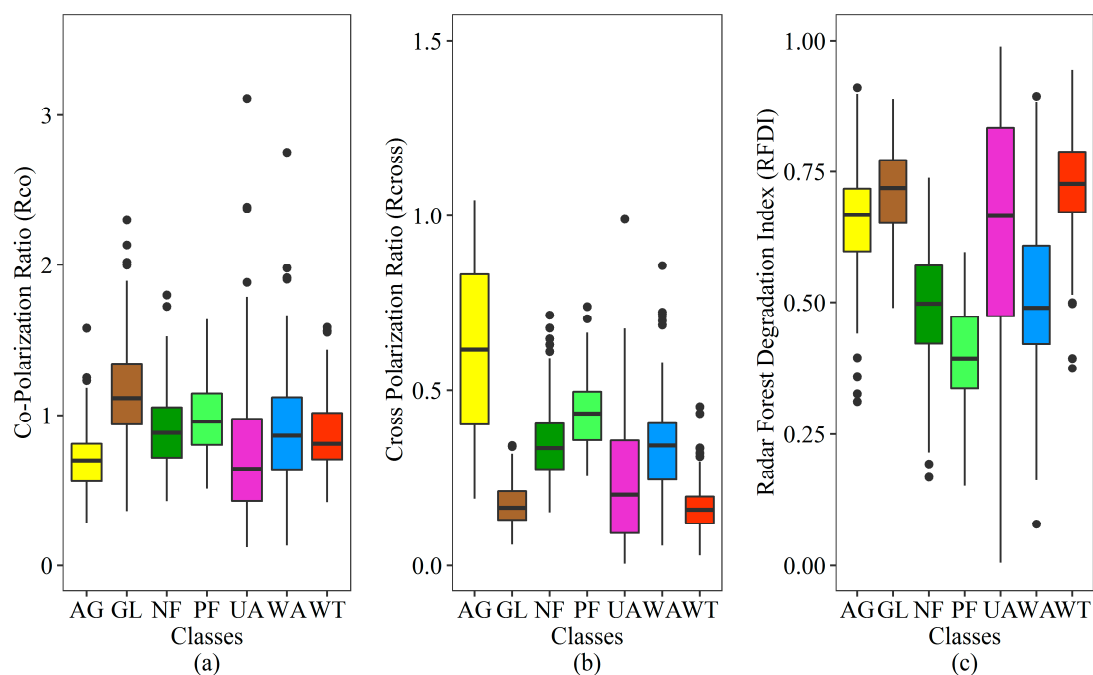


**Figure 7.** Boxplot graph of the selected land cover classes of the attributes Rco (a), Rcross (b), and RFDI (c). The description of the classes is in Table 3.

Analyzing the Cross-Polarization Ratio (Rcross) attribute (Figure 7b) for the land cover classes, class AG showed the highest average value for this attribute with 0.617, presenting a greater potential to discriminate this class, with a greater contribution from the superficial scattering in relation to volumetric. Analyzing the average values obtained for the attribute Radar Forest Degradation Index (RFDI) (Figure 7c), the classes WT (0.717), GL (0.709), AG (0.652), and UA (0.642) presented higher values compared to the other land cover classes. This attribute has a greater sensitivity to distinguish areas with little green biomass [38].

From the values of the Alpha-Entropy decomposition attributes presented in the boxplot graphs of Figure 8, it can be analyzed that the classes PF, NF, WA, and UA present the highest mean values of alpha angle (Figure 8a), with values close to  $45^\circ$ , featuring a volumetric scattering. The highest mean value recorded in the Anisotropy attribute (A) (Figure 8b) was for the UA class (0.475). The reduced number of complex scatters (branches and leaves) contributes to the signal's low depolarization or the low volumetric scattering mechanism. Therefore, surface scattering and double-bounce mechanisms are highlighted in this class [59]. For the Entropy attribute (H) (Figure 8c) the PF, NF, and WA classes presented high average values of 0.888, 0.854, and 0.826, respectively, compared to the other classes. Higher entropy values (H) are expected in more complex targets and with a well-developed geometric structure [59,60].

Figure 9 shows the two-dimensional Entropy plane (H) and alpha angle proposed by Cloude and Pottier [40], showing different backscattering mechanisms for the classes analyzed. The WT class presented average H values, and most of the alpha angle values were less than  $45^\circ$ . With these results, the class covered zone 5, presenting vegetated surfaces, zone 6, reflecting the increase in entropy due to changes in surface roughness and the effects of canopy propagation, and zone 9, corresponding to a superficial scattering that characterizes water in the L band. It can be observed that the PF and NF classes reached high and medium H values and alpha angle values greater than  $45^\circ$ , covering the mechanisms of scattering vegetation layers with a well-developed geometric structure and scattering of vegetated surfaces, characteristics of zones 1, 2, 4, and 5. The GL class is distributed in zones 5, 6, and 9, covering surface scattering mechanisms with medium and low H and alpha angle values less than  $45^\circ$ .

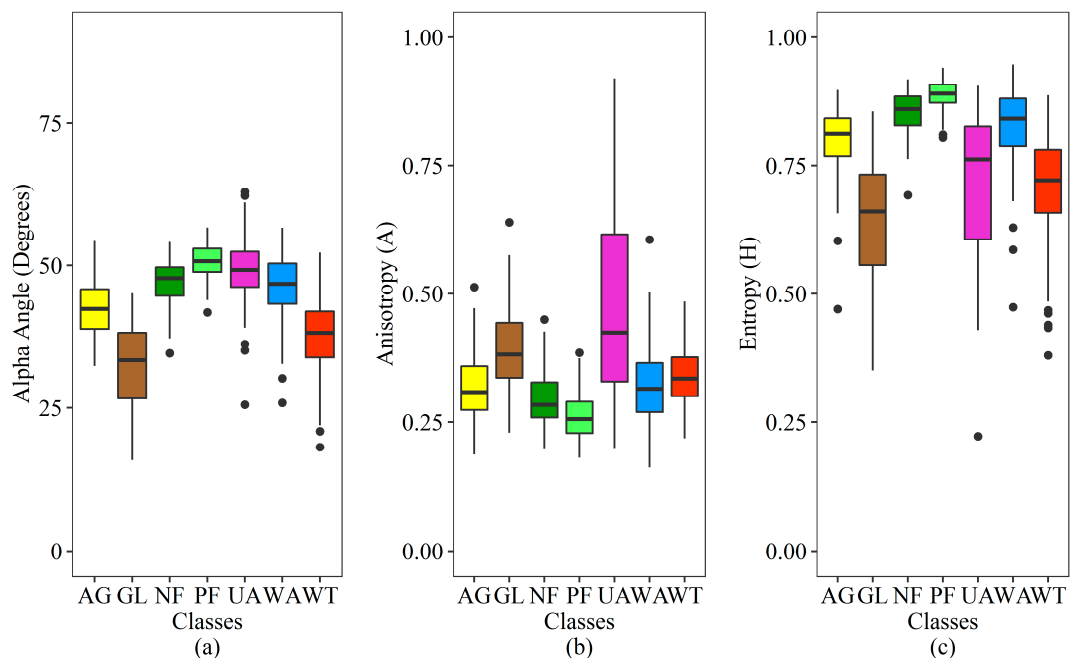


**Figure 8.** Boxplot plot of land cover classes of the alpha angle (a), anisotropy (b), and entropy (c) attributes of the Cloude-Pottier decomposition. The description of the classes is in Table 3.

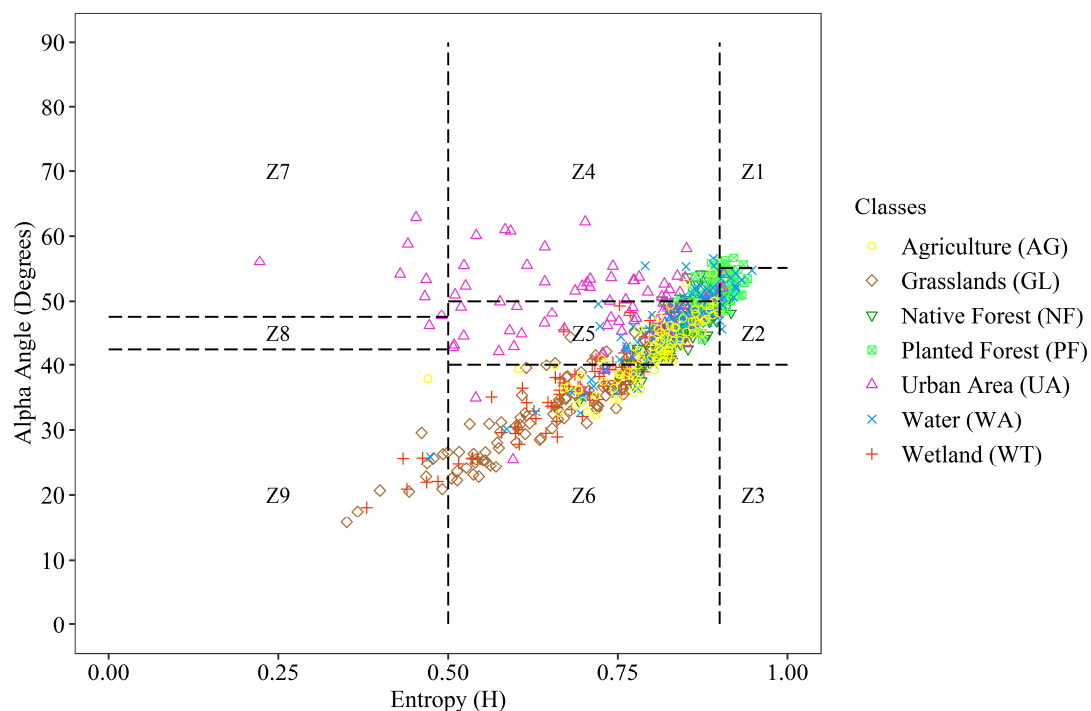


**Figure 9.** Two-dimensional plane of entropy and alpha angle.  $Z_i$  = zones established by Cloude and Pottier [40].

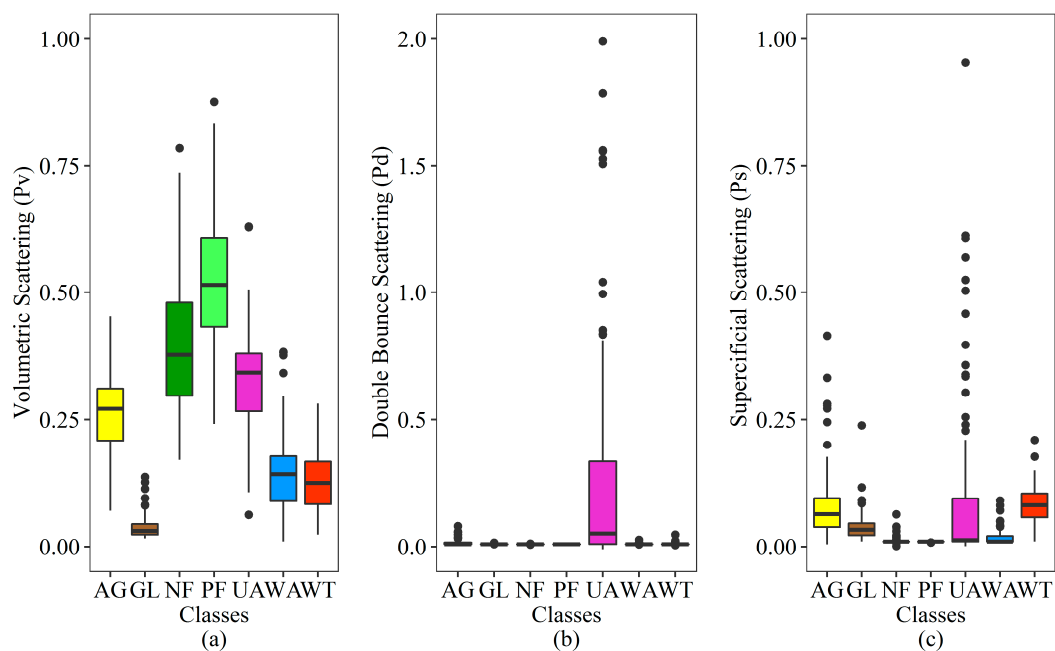
The UA class is distributed in zones 2, 4, and 5. It presents high and medium H values due to the predominance of the double-bounce scattering mechanism. However, some values are also distributed in zones 6, 7, and 8, with predominance of surface scattering mechanisms due to its medium and lower H. The high variability reported for this specific land cover class is well in agreement with the spectral profiles shown in Figure 2.

The WA class is mainly distributed in zones 5 and 6, with characteristics of a surface scattering. Class AG is distributed in zone 5 and it presents scattering with average H and

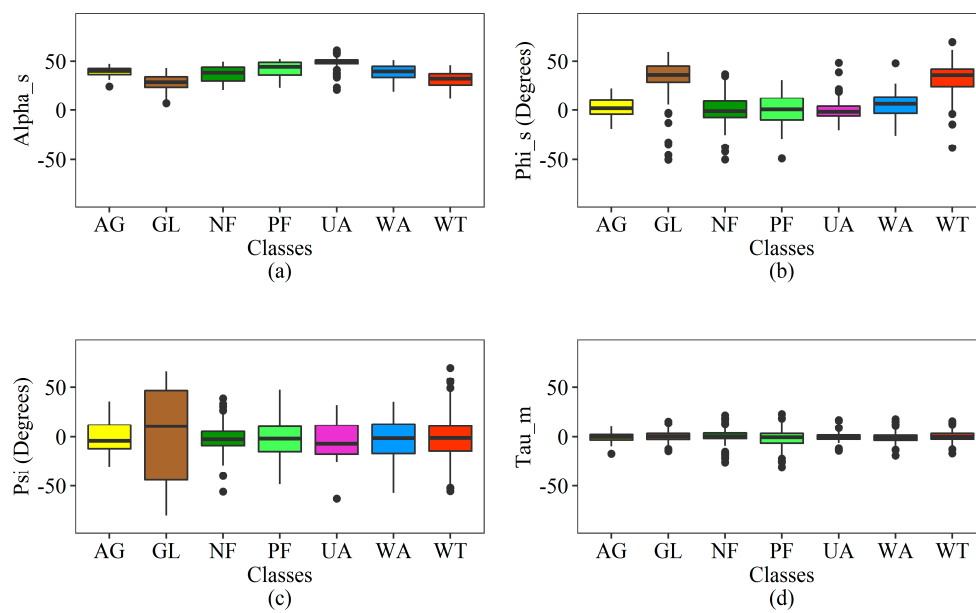
anisotropic scatters. These results show that the scattering mechanisms identified through the two-dimensional plane are in accordance with the classes described and analyzed in this study.

Figure 10 presents the boxplot graphs of the values of the decomposition attributes of Freeman and Durden. Analyzing the Pv attribute (Figure 10a), the PF and NF classes with high green biomass were the land cover classes that showed a high average value for this attribute with a magnitude of 0.520 and 0.401 heightened discrimination capacity of these classes. For the Pd attribute (Figure 10b), the UA class had the highest values, as previously mentioned. This class has a predominance of corner reflections related to buildings' presence, highlighting the ease of discrimination of this class in this attribute. In the Ps attribute (Figure 10c), the classes that presented the highest values were the UA (0.098) and WT (0.082) classes, with a superficial backscattering characteristic, with a greater potential for discrimination in this attribute.

As shown in Figure 11a, the alpha\_s angle of the Touzi decomposition presented very similar responses with values close to  $45^\circ$  considering multiple scattering. The class that obtained the highest response for this attribute was the UA class ( $48.6^\circ$ ). The Phi angle (Figure 11b) showed the greatest potential to separate the classes WT and GL from the other classes, presenting intermediate values close to  $45^\circ$ , indicating that the scattering is derived from multiple interactions [41]. For the Psi angle, the highest mean value was for the GL class (2.802). The other classes presenting values very close to zero indicate that there is a low target rotation. The Tau angle presents very similar responses for all cover classes, with values close to zero, indicating that the targets have symmetrical scattering [41].



**Figure 10.** Boxplot graph of the land cover classes of the volumetric (a), double bounce (b) and superficial (c) attributes of the Freeman and Durden decomposition. The description of the selected land cover classes is in Table 3.



**Figure 11.** Boxplot graph of the land cover classes of the alpha\_s (a), phi\_s (b), psi (c), and tau\_m (d) attributes of the Touzi decomposition. The description of the land cover classes is in Table 3.

### 3.3. Classification of Land Cover Classes in Different Data Input Models

In Figure 12, it is possible to visually analyze the difference in classification accuracy from Model 1 (M1) (Figure 12b) to Model 6 (M6) (Figure 12c), which are the extreme data input models that present only SAR input data. M6 showed a greater discrimination capacity of the land cover classes than the M1, emphasizing the WT, WA, AG, and NF (Figure 13a,b; Table A1).

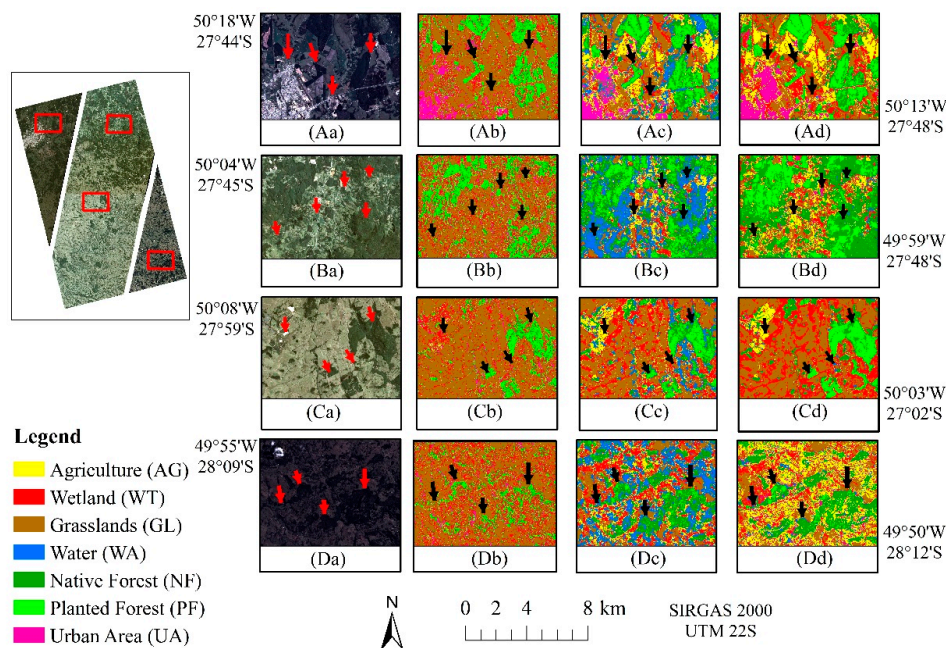


**Figure 12.** Classification of the selected land cover classes: Upper left (A), Upper right (B), Central (C) and Lower right (D) subsets; PlanetScope image (a); Models M1 (b), M6 (c) and M9 (d). The areas in this figure are subsets of Figure 1d and the classifications of models M1, M6, and M9 to show more details of the mapping and indicate areas with the main changes identified along the classifications through arrows. The description of acronyms and models is in Table 4.

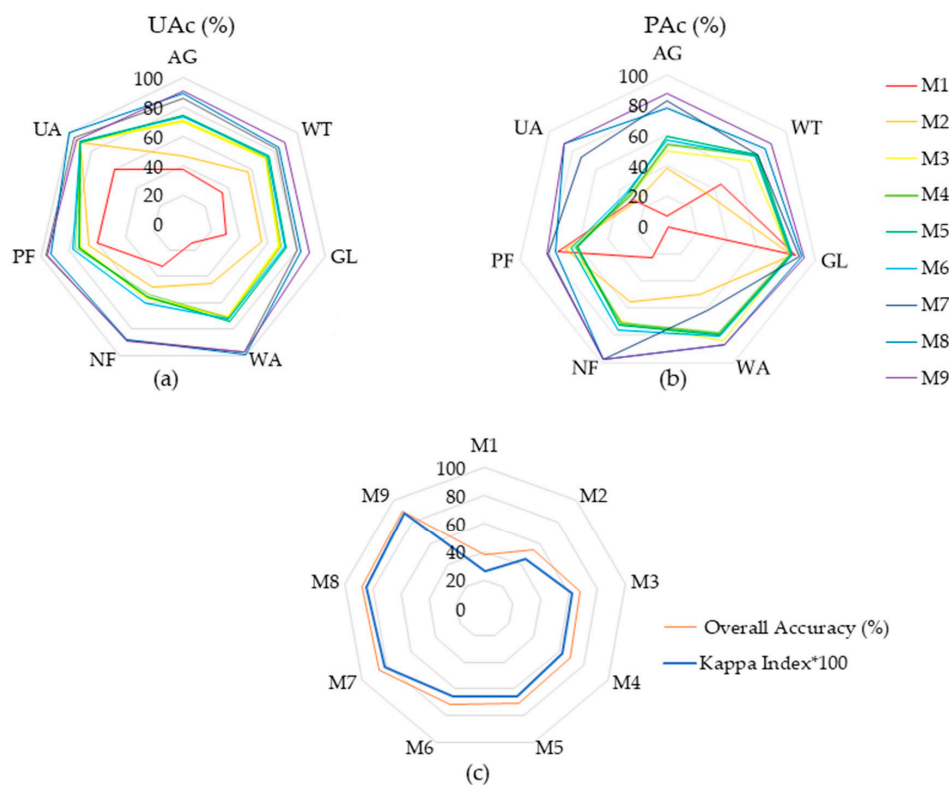


**Figure 13.** Classification accuracy of the nine different data input models considering the weight of the land cover classes: User Accuracy (UAc%) (a); Producer accuracy (PAc%) (b); Overall classification accuracy and Kappa Index (c). The description of the land use classes is in Table 3 and the description of acronyms and data input models in Table 4.

M1 data input model presents only the intensity backscattering coefficients of the studied polarizations (HH, HV, VH, and VV). The M6 presents the  $\sigma^0$  data added with the polarimetric features. The initial values achieved for the overall accuracy and Kappa index were 37.48% and 0.26 in M1. It increased to 71.35% and 0.66 for M6 (Figure 13c; Tables 5 and A1). Therefore, the addition brought an increase of 90.36% and 53.84% for the global accuracy and Kappa index, respectively. This increase was also significant for the Z-test (Table 6). In summary, the reported results corroborate well with the studies carried out by Zou et al. [61], Longepe et al. [62], Mishra et al. [31] and Liesenberg et al. [21], showing that the classification accuracy of specific land use and land cover classes tends to increase from a single dataset for the complementary use of parameters derived from SAR data. This aspect reveals the relevance of polarimetric attributes for mapping initiatives.

The increasing performance from M1 to M6 is also confirmed by the results presented in Figure 13a,b. In both Figure 13c and Table A1, which shows the user and producer accuracy, the land cover classes showed an increase in the classification accuracy with the increase of the polarimetric attributes. In general, M6 presented a good individual class classification accuracy since most classes achieved user accuracy and producer accuracy above 70% (Figure 13c, Table A1). The UA class presented the highest user accuracy with 90.36%, whereas the GL reached the highest producer accuracy, with 84.15%. These measures would be an interesting data source for monitoring specific land cover classes in the study region because these areas are often affected by cloud coverage.

**Table 5.** Summary of the Weighted Overall Accuracy (a) and Kappa index (b) results for each of the nine data input models with the standard error and upper and lower limit scores at a 95% confidence interval.

<b>(a) Weighted Overall Accuracy</b>									
	<b>M1</b>	<b>M2</b>	<b>M3</b>	<b>M4</b>	<b>M5</b>	<b>M6</b>	<b>M7</b>	<b>M8</b>	<b>M9</b>
<b>OA</b>	0.3748	0.5393	0.6843	0.6920	0.7080	0.7135	0.8556	0.8744	0.9029
<b>Var(OA)</b>	0.0003	0.0004	0.0003	0.0003	0.0003	0.0003	0.0003	0.0002	0.0002
<b>Lower limit</b>	0.3396	0.5004	0.6480	0.6561	0.6727	0.6782	0.8233	0.8448	0.8770
<b>Upper limit</b>	0.4100	0.5781	0.7206	0.7279	0.7433	0.7489	0.8879	0.9040	0.9288
<b>(b) Weighted Kappa Index</b>									
	<b>M1</b>	<b>M2</b>	<b>M3</b>	<b>M4</b>	<b>M5</b>	<b>M6</b>	<b>M7</b>	<b>M8</b>	<b>M9</b>
<b>Kappa</b>	0.2638	0.4520	0.6242	0.6333	0.6522	0.6587	0.8177	0.8439	0.8804
<b>Var(K)</b>	0.0002	0.0002	0.0003	0.0003	0.0003	0.0003	0.0003	0.0003	0.0003
<b>Lower limit</b>	0.2363	0.4214	0.5930	0.6020	0.6209	0.6273	0.7817	0.8095	0.8464
<b>Upper limit</b>	0.2912	0.4826	0.6555	0.6646	0.6836	0.6900	0.8537	0.8784	0.9144

**Table 6.** Z-test scores applied to the Kappa index of the nine different data input models.

	<b>M1</b>	<b>M2</b>	<b>M3</b>	<b>M4</b>	<b>M5</b>	<b>M6</b>	<b>M7</b>	<b>M8</b>	<b>M9</b>
<b>M1</b>	-	8.97	16.99	17.40	18.27	18.57	23.99	25.80	27.66
<b>M2</b>	-	-	7.72	8.12	8.96	9.24	15.17	16.66	18.35
<b>M3</b>	-	-	-	0.40 <sup>1</sup>	1.24 <sup>1</sup>	1.52 <sup>1</sup>	7.96	9.26	10.88
<b>M4</b>	-	-	-	-	1.92	1.12 <sup>1</sup>	7.58	8.87	10.48
<b>M5</b>	-	-	-	-	-	0.28 <sup>1</sup>	6.80	8.06	9.67
<b>M6</b>	-	-	-	-	-	-	6.53	7.79	9.40
<b>M7</b>	-	-	-	-	-	-	-	1.03 <sup>1</sup>	2.48
<b>M8</b>	-	-	-	-	-	-	-	-	1.48 <sup>1</sup>

<sup>1</sup> Non-significant difference for 95% confidence level with a critical value of 1.96 and the description of acronyms and models is in Table 4.

Although still showing satisfactory overall classification accuracy and Kappa indices (Figure 13c; M1 to M6), the additional use of SAR derived texture applied over the intensity backscattering coefficients would indeed render an increase of the classification accuracy scores. This initiative was reported recently by Attarchi [63] when studying different urban environments with a single date acquisition of the quad-polarization ALOS/PALSAR. Interestingly would be the use of seasonal SAR quad-polarization in the classification scheme. Seasonal aspects were also considered by Furtado et al. [8] and more recently by Guimarães et al. [64] in the discrimination of complex environments containing wetlands.

Alternatively, the addition of interferometric coherence that can be explored from two or more SAR acquisitions sounds also like the right choice for future studies, as reported by Pulella et al. [65]. However, multitemporal quad-polarization ALOS/PALSAR-2 datasets are unfortunately still not available for the specific study area and are therefore encouraged for further studies once they become available.

The use of SENTINEL-2A data alone (M7) performed well with a weighted overall accuracy and Kappa index of 85.56% and 0.874, while M6 performed with 71.35% and 0.66, respectively (Tables 5 and A1). This increase was also significant for the Z-test (Table 6) and resulted from a substantial increase in user accuracy and producer accuracy for almost all selected land cover classes. The use of SENTINEL-2A would indeed render the best classification reports. However, in the absence of optical images, ALOS/PALSAR-2 could also reach satisfactory results, mainly for WT and GL what could be of interest for ecological

studies. Besides these two vegetation physiognomies, monitoring UA and its expansion in this specific region are also recommended to prevent houses' construction in irregular areas, such as those affected by flooding events.

Interestingly would-be monitoring initiatives of both the WT and GL that are currently suffering from land conversion into planted forest and agriculture. The region is known as being one of the last agricultural frontiers in Southern Brazil. The gentle topography allows using agricultural machinery intensively. The monitoring in specific timeframes in the so-called cloud coverage period, which coincides with the mowing and plowing events, would surely hinder the conversion of these specific physiognomies into agriculture and facilitate earlier interventions and administrative fines by the environmental policy. More recently, some SAR initiatives reported using SAR coherence time-series to target these particular agricultural activities with relative success [66]. This practice is strongly recommended for the specific study area in the near future. This procedure could consider plotting such locations with the georeferencing of rural properties' compulsory initiative of the Brazilian Government, which has the primary purpose of locating each rural property within the Brazilian Geodetic System (SGB).

It can be seen in Figure 13c and Table 5 that throughout the addition of the polarimetric attributes and the optical data in the respective models, it tends to increase the values of global accuracy and Kappa index. However, the addition of SAR-derived features to SENTINEL-2A, such as M8 and M9 datasets, slightly improved the overall classification accuracy. In summary, it did not bring many advantages in this particular study (Table 6). The classification of M9 (Figure 12d), which presents all the data of the polarimetric attributes and the optical data, shows slightly discriminatory potential for the land cover classes compared with the optical image outcomes alone (M7). Although obtaining a better delimitation of the selected land cover classes compared to the other classifications, the slight improvements were not significant at a 95% confidence level (Tables 5 and 6). The exception occurs very marginally for the M9, although both upper and lower limits for overall accuracy and Kappa indices of M7 still overlap. Such results did not follow the results achieved by Mendes et al. [4], Pereira et al. [20], and Liesenberg et al. [21]. These studies showed a significant increase in land cover classes' classification accuracy by combining SAR and optical data. Possible reasons for that behavior would most probably be related to a large amount of precipitation recorded prior to SAR data acquisition that coincides with this specific area's rainy season period.

M8 and M9 present a weighted overall classification accuracy of 87.44% and 90.29% and a weighted Kappa index of 0.84% and 0.88%. Although the M8 and M9 models do not significantly differ in classification accuracy values, the M9 model showed slightly better discrimination, mainly of the AG, WT, and GL classes compared to the M8 model. However, when M6 is compared with M8 or even M9 directly, the increase in overall accuracy is 22.55% and 26.54%. Whereas for the Kappa index, it is 27.27% and 33.33%, respectively.

Figure 14 and Table 7 show the percentage of coverage of the analyzed land use and occupation classes. It can be interpreted that in the classification of the M1 model, the GL class has the largest coverage area. As the polarimetric attributes were added, the GL pixels were then assigned to other classes. It shows that additional features from SAR are necessary to label this specific land cover class and other physiognomies correctly.

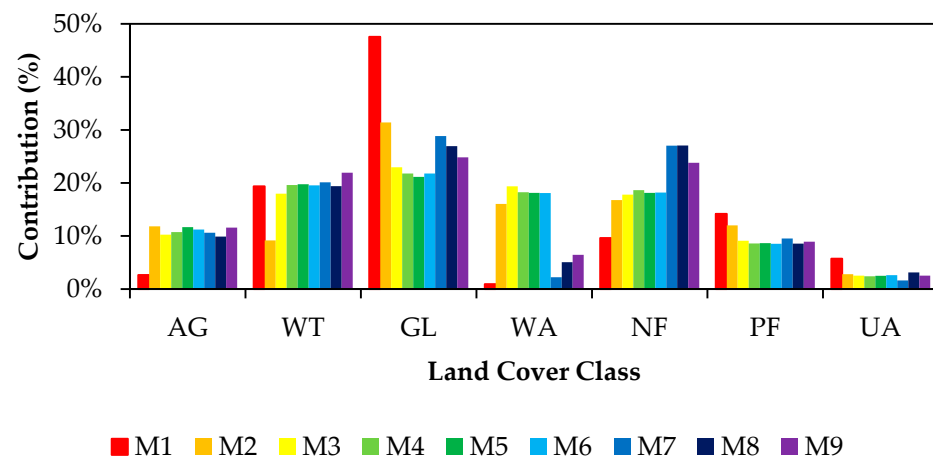


**Figure 14.** Percentage of coverage of the seven land cover classes in nine different data input models. The classes' description is in Table 3. The description of acronyms and models in Table 4.

It can be analyzed that in the M6 model, which was the model with the highest overall classification accuracy and Kappa index, it showed that the classes GL (21.79%), WT (19.55%), NF (18.20%), and WA (18.10%) presented the most significant percentage of land cover classes (Figure 14 and Table 7). M6 is the data input dataset that contains only SAR data.

In general, M9 obtained the highest Kappa index and overall accuracy compared to other models. It presents the combination of polarimetric attributes with optical data, and it was observed that the GL classes (24.84%), NF (23.79%), and WT (21.92%) continue to be the land cover classes with the highest coverage in the study area. However, the WA class (6.44%) showed a reduction in land cover percentage than the M6 model. The results confirmed both GL and WT as the most representative land cover classes in the study area. Such findings corroborate with previous studies conducted by Magalhães et al. [22], Pôlese et al. [23], and Almeida et al. [67]. These researchers conducted local studies in this specific region and reported the large presence of native grasslands and wetlands.

**Table 7.** Area and percentage of the land cover classes in each data input model.

Classes	M1		M2		M3	
	Area (km <sup>2</sup> )	% land cover	Area (km <sup>2</sup> )	% land cover	Area (km <sup>2</sup> )	% land cover
AG	77.47	2.64	347.13	11.81	301.00	10.24
WT	569.43	19.38	268.92	9.15	528.30	17.98
GL	1397.71	47.57	922.78	31.40	674.80	22.96
WA	26.91	0.92	471.54	16.05	569.22	19.37
NF	282.41	9.61	493.20	16.78	523.24	17.81
PF	416.28	14.17	352.81	12.01	267.30	9.10
UA	168.25	5.73	82.09	2.79	74.60	2.54
Total	2938.47	100.00	2938.47	100.00	2938.47	100.00

Table 7. Cont.

Classes	M4		M5		M6	
	Area (km <sup>2</sup> )	% land cover	Area (km <sup>2</sup> )	% land cover	Area (km <sup>2</sup> )	% land cover
AG	315.04	10.72	342.79	11.67	329.39	11.21
WT	575.82	19.60	580.98	19.77	574.44	19.55
GL	640.47	21.80	621.06	21.14	640.20	21.79
WA	536.39	18.25	533.16	18.14	531.91	18.10
NF	547.41	18.63	532.38	18.12	534.82	18.20
PF	252.24	8.58	254.45	8.66	250.90	8.54
UA	71.11	2.42	73.65	2.51	76.82	2.61
Total	2938.47	100.00	2938.47	100.00	2938.47	100.00
Classes	M7		M8		M9	
	Area (km <sup>2</sup> )	% land cover	Area (km <sup>2</sup> )	% land cover	Area (km <sup>2</sup> )	% land cover
AG	312.06	10.62	290.25	9.88	340.20	11.58
WT	591.14	20.12	569.74	19.39	644.20	21.92
GL	847.41	28.84	791.72	26.94	729.80	24.84
WA	65.54	2.23	148.45	5.05	189.27	6.44
NF	794.10	27.02	795.35	27.07	699.20	23.79
PF	280.16	9.53	251.22	8.55	261.90	8.91
UA	48.07	1.64	91.75	3.12	73.90	2.51
Total	2938.47	100.00	2938.47	100.00	2938.47	100.00

### 3.4. Importance of Features for Classification Accuracy

The features that most contributed to the classification of M6 and M9 are shown in Table 8 and Figure 15a,b, respectively. The feature that most contributed to the classification accuracy of the M6 model was the volume dispersion contribution (Pv), representing 40.88% of the classification accuracy, as can be seen in Figure 15a. This feature presents a high discrimination capacity of the selected land cover classes, mainly classes with dense vegetation. This is due to the multiple scattering processes that occur in cover classes. It can be analyzed in Table 8 that after adding the second feature (Double-bounce dispersion contribution (Pd)) in the classification of Model M6, the classification accuracy increased to 55.77%. As shown in Figure 14 and Table 7, the M1 model considered a large area of land occupation for the CP class, and as the features were added, the pixels of this class are correctly classified. As noted in Table 8 and Figure 15a, the main features that influenced this result were the geometric attributes such as Pv and Pd for M6.

Analyzing Table 8 and Figure 15b, the feature that most contributed to the classification of the M9 model was the B12 band (SWIR-2), providing a classification accuracy of 47.50% and, after adding the feature Pv, the classification accuracy increased to 69.01%. Interestingly is the role of both NIR and red-edge spectral bands ranked in third and fifth places corroborating with previous spectral analysis shown in Figure 4c. For the M6 and M9 models classification, the first six variables already provided the highest classification accuracy. It can be seen in Figure 15 that the global accuracy increases if more features are included in the classification until an ideal number of features is reached, after which the accuracy remains constant. Similar features from either SAR or optical datasets were also reported in the studies of Pal and Foody [68], Rabe et al. [69], Waske et al. [70], and van Beijma [71].

According to the results presented, the exclusive use of different polarimetric attributes from ALOS/PALSAR-2 data have potential use in mapping specific land cover types of Santa Catarina Southern Plateau. It shows the importance of using this type of data for mapping initiatives at the regional level where a large cloud coverage during the year exists, as in the Santa Catarina Southern Plateau.

Although not statistically significant compared with optical images alone, the combined use of SAR data with the optical images must be further investigated. Unfortunately, the P band is still not available on the orbital level to allow further investigations. Similarly, the quad-polarization acquisition mode at L band SAR systems acquired on regular intervals covering both rainy and dry seasons is still limited for complementary studies.

**Table 8.** Contribution of features to the SVM supervised classification of M6 and M9.

Classification	M6		M9	
	Feature	Overall Acc.	Feature	Overall Acc.
1	Pv	40.88	B12	47.5
2	Pd	55.77	Pv	69.01
3	A	65.83	B8A	79.17
4	$\alpha_s$	69.22	Ps	83.47
5	$\phi_{\alpha s}$	70.85	B05	85.92
6	HH	72.3	B11	87.74
7	Rcroos	72.59	RFDI	88.73
8	VV	73.68	$\alpha_s$	89.14
9	H	73.75	B07	89.46
10	$\Delta(\text{HH-HV})$	74.02	H	89.71
11	HV	74.19	B4	90.06
12	Pd	74.21	B2	90.13
13	$\alpha$	74.69	VV	90.24
14	VH	74.9	$\alpha$	90.48
15	$\tau_m$	75.24	VH	90.65
16	$\Delta(\text{HV-VV})$	75.09	$\Delta(\text{HH-VV})$	90.6
17	RFDI	74.82	Pd	90.42
18	$\Psi$	74.22	Rcroos	90.5
19	$\Delta(\text{HH-VV})$	74.38	$\Delta(\text{HH-HV})$	90.38
20	Rco	73.7	B06	90.34
21	-	-	$\tau_m$	90.57
22	-	-	$\phi_{\alpha s}$	90.51
23	-	-	A	90.54
24	-	-	$\Psi$	90.26
25	-	-	$\Delta(\text{HV-VV})$	89.89
26	-	-	Rco	89.65
27	-	-	HV	89.78
28	-	-	B03	89.68
29	-	-	B08	89.49
30	-	-	HH	89.75

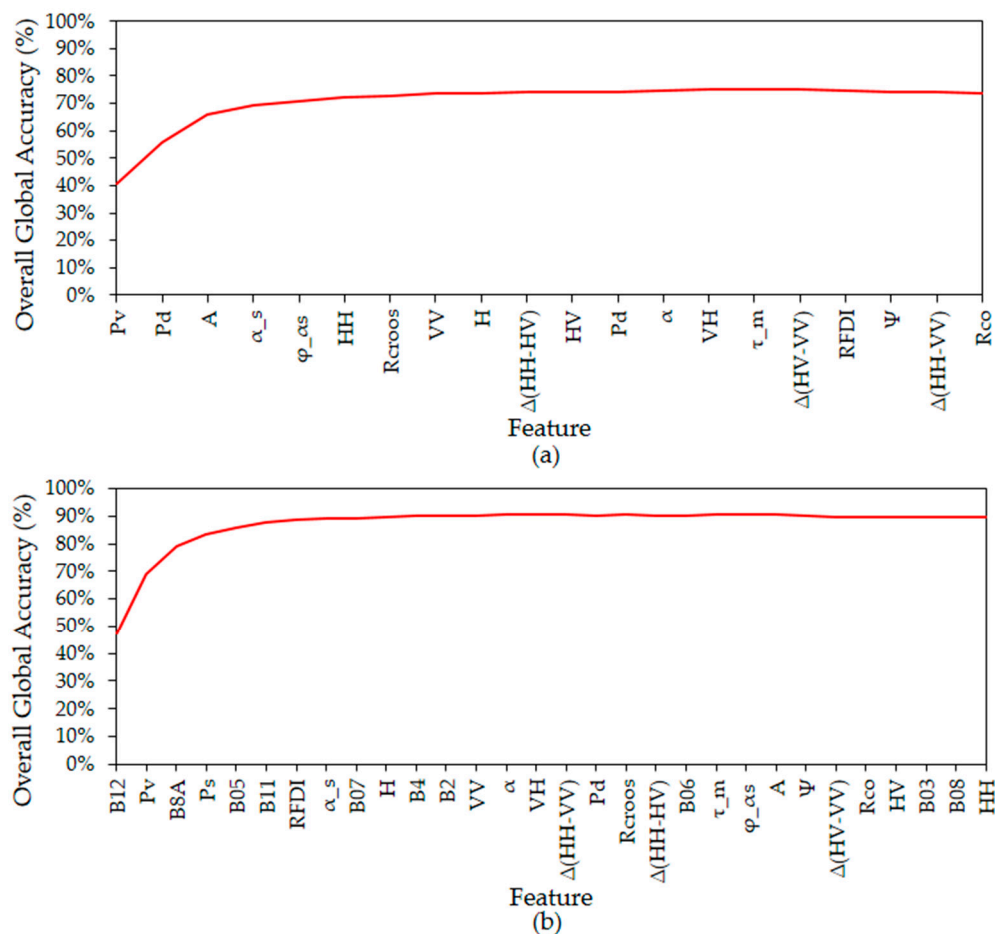


**Figure 15.** Contribution of features to the classification of the M6 (a) and M9 (b) model. The description of the features is in Table 4.

Additional experiments can be conducted exploring different sizes of training and validation datasets. Varying the size of both training and validation datasets according to the spatial representativeness of each of the land cover classes in the given landscape is also an important aspect that could be evaluated as reported by Olofsson et al. [48].

Alternatively, reducing the number of land cover classes in the classification scheme by applying masks and focusing only on those land cover classes that are very similar in terms of horizontal and vertical structures would also help to achieve better results.

Although SVM is a reliable approach in classification, as shown in this research, it will be more useful if the results are compared by other recent classification algorithms such as random forest, convolutional neural network (CNN), and eXtreme Gradient Boosting (XGBoost). Public domain libraries like Scikit-learn and TensorFlow provide a simple way for this operation and are also suggested for further studies.

### 3.5. Further Research Perspectives

According to the results found in this study, there are some perspectives for future studies. Much of the research using ALOS/PALSAR-2 full polarization and experimental data is used to map land cover in the Amazon region due to the intense cloud cover during most of the year. However, this type of data's potential also needs to be explored in other environments affected by frequent cloud coverage. Besides, it is still vague to develop studies to combine multiple sensors in southern Brazil.

It is recommended to use other SAR sensors in full and dual experimental mode for mapping the land cover, such as the TerraSAR-X satellite, launched in June 2007, and the Tandem-X satellite, launched in June 2010. These two systems feature sensors operating

in the X band. Hence, small satellites for the Mediterranean basin observation COSMO-SkyMed consist of four SAR systems at X band acquiring data at single or dual-polarization.

The RADARSAT Constellation Mission (RCM), a constellation of 3 satellites launched in 2019, provides continuity of C band SAR data for RADARSAT-2 users. This mission mainly collects data from Canada with a daily revisit and has daily access to 95 % of the Earth's surface. Additionally noteworthy is the Sentinel-1 mission, which consists of two satellites, Sentinel-1A, launched in 2014, and Sentinel-1B, launched in 2016, operating in band C. It is also recommended to develop research aimed at analyzing the potential of using multi-frequency SAR data to discriminate land use and land cover classes. Still, it is important to emphasize the need to elaborate works analyzing the possibility of integrating Sentinel-1 data with Sentinel-2 data to map land cover.

Research involving the use of SAR data combined with Light Detection and Ranging (LiDAR) data can assist in discriminating land cover classes, such as LiDAR data provided by the GEDI (Global Ecosystems Dynamics Investigation Lidar) instrument, launched in December 2018. This instrument offers a complete 3D view, in high resolution, of the Earth's forests. Complementary, the data made available by the ICESat-2 satellite, which measures the variation in the Earth's ice thickness, as well as characteristics of the topography and terrestrial vegetation, launched in September 2018.

A future perspective to assist in mapping land cover using SAR data is in the use of satellite images that are yet to be launched, such as the Tandem-L mission concept that is based on the use of two SAR satellites operating in L-band and planned to be launched in 2024. Interestingly, the NISAR satellite (NASA-ISRO SAR) whose launch is scheduled for December 2021. It is an InSAR (Interferometric SAR) mission from the USA and India dedicated to studying global environmental hazards and changes. NISAR will be the first satellite mission to use two different SAR frequencies (L and S bands). In addition to this, the BIOMASS satellite is scheduled for launch in 2021, which will take the first SAR in the P band that has been showing the most accurate land cover mapping initiatives. The mission aims to carry out forest biomass measurements to assess stocks and flows of terrestrial carbon to understand the carbon cycle better.

#### 4. Conclusions

This study showed that the full polarimetric images of ALOS/PALSAR-2 are satisfactory in discriminating the classes of land use and occupation in the Santa Catarina Southern Plateau region. These classes' classification accuracy has improved significantly with incorporating different polarimetric features derived from the intensity backscattering coefficients and phase information that were also important ranked features in SVM classification.

The sole use of intensity backscattering coefficients had an overall accuracy of 37.48% and a Kappa index of 0.26. The addition of polarimetric features increased it to 71.35% and 0.66, respectively. Although the scores are not very high, the use of parameters derived only from SAR data presents itself as an interesting alternative for the discrimination of specific land cover classes such as grasslands and wetlands. This is especially true when clouds frequently cover a particular environment or no optical data is available in the region.

SENTINEL-2A data alone outcome all experiments with an overall accuracy and Kappa index of 85.56% and 0.82, respectively. It resulted from a significant increase in user accuracy and producer accuracy for almost all selected land cover classes. It also overcomes the performance of the SAR dataset according to the Z-test.

Interestingly, the addition of SAR-derived features into the optical dataset slightly improved overall classification accuracy. However, statistically, it was not significant. Possible implications for that performance are the accumulated precipitation prior to SAR data acquisition, which coincides with the study area's rainy season. Therefore, new experiments are required to confirm the results.

In this sense, new experiments are still necessary to increase classification accuracy, indicating the advantages of integrating more SAR features such as texture and interferometric coherence. In this way, this research can help public agencies to improve methodologies for mapping specific land cover classes at the regional level. This is especially true in periods where clouds' occurrence is high, and information about unauthorized agriculture practices over grasslands, wetlands, and native forests is required regularly.

**Author Contributions:** Conceptualization, V.L. and J.d.S.C.; methodology, V.L., M.B.S., P.d.C.B. and A.R.G.; software, V.L. and J.d.S.C.; validation, V.L., S.L.R.N. and J.d.S.C.; formal analysis, A.R.G., R.V.d.S. and P.d.C.B.; investigation, J.d.S.C., V.L., P.d.C.B. and A.R.G.; resources, J.d.S.C., and V.L.; data curation, J.d.S.C. and M.B.S.; writing—original draft preparation, J.d.S.C. and V.L.; writing—review and editing, J.d.S.C., V.L., M.B.S., E.M. and L.J.B.; visualization, J.d.S.C., V.L., M.B.S., R.V.d.S., L.J.B., A.R.G., S.L.R.N., E.M. and P.d.C.B.; supervision, V.L., R.V.d.S. and M.B.S.; project administration, J.d.S.C. and V.L.; funding acquisition, V.L. All authors have read and agreed to the published version of the manuscript.

**Funding:** This research was partially funded by the Santa Catarina Research Foundation (FAPESC; 2017TR1762, 2019TR816), and the Brazilian National Council for Scientific and Technological Development for individual supports (CNPq; 307689/2013-1; 313887/2018-7; 436863/2018-9).

**Institutional Review Board Statement:** Not applicable.

**Informed Consent Statement:** Not applicable.

**Data Availability Statement:** The data presented in this study are available on request from the corresponding author. The data are not publicly available due to JAXA and Planet Labs data policy.

**Acknowledgments:** We would like to thank the Graduate Program of Forest Engineering of the State University of Santa Catarina (UDESC) to support the master thesis of the first author and the Coordination for the Improvement of Higher Education Personnel (CAPES). We would also like to thank the owners of the rural properties located in the study site to allow us the local access. Copernicus program for making available Sentinel-2 imagery, Planet Labs for the courtesy in providing the PlanetScope imagery and the Japan Aerospace Exploration Agency (JAXA), under ALOS Research Announcement (Process 1090), which provided the ALOS/PALSAR-2 data. Finally, we would like to thank the editors and three reviewers for providing constructive concerns and suggestions. Such feedback helped us improve the quality of the manuscript.

**Conflicts of Interest:** The authors declare no conflict of interest. The funders had no role in the study's design; in the collection, analyses, or interpretation of data; in the writing of the manuscript, or in the decision to publish the results.

## Appendix A. Methods and Results



(a)



(b)

**Figure A1.** Landscape overview of the study area with detail to grassland (GL), wetland (WT) and planted forest (*Pinus taeda*) in the back view (a) and grassland (GL), agriculture (AG) and native forest (NF) with predominant *Araucaria angustifolia* trees (b).

**Table A1.** The classification accuracy results in terms of weighted User' Accuracy (UA<sub>c</sub>) and Producer' Accuracy (PA<sub>c</sub>) for the seven land cover classes and the nine different data input models. The weighted Overall Accuracy (OA) and Kappa index (K) are also shown.

Classes	M1		M2		M3	
	UA <sub>c</sub> (%)	PA <sub>c</sub> (%)	UA <sub>c</sub> (%)	PA <sub>c</sub> (%)	UA <sub>c</sub> (%)	PA <sub>c</sub> (%)
AG	37.50	6.49	46.55	38.67	70.45	50.03
WT	34.42	44.67	57.33	34.25	72.83	69.56
GL	30.80	86.69	55.32	84.74	67.72	82.73
WA	14.29	0.82	44.92	49.89	71.07	84.51
NF	32.14	23.35	48.31	55.78	55.88	69.40
PF	60.14	73.98	66.40	69.14	72.17	65.55
UA	60.00	27.95	90.16	26.68	90.00	31.26
OA (%)	37.48		53.93		68.43	
K (%)	0.26		0.45		0.62	
Classes	M4		M5		M6	
	UA <sub>c</sub> (%)	PA <sub>c</sub> (%)	UA <sub>c</sub> (%)	PA <sub>c</sub> (%)	UA <sub>c</sub> (%)	PA <sub>c</sub> (%)
AG	74.42	54.39	73.91	59.14	73.63	57.08
WT	73.00	74.68	75.26	76.05	74.23	74.64
GL	69.60	83.29	72.36	84.06	71.54	84.15
WA	71.30	78.65	73.87	79.96	72.17	80.43
NF	54.05	71.24	55.45	72.55	60.36	76.24
PF	75.47	61.92	72.90	60.57	77.14	64.67
UA	90.24	32.05	89.41	33.80	90.36	35.04
OA (%)	69.20		70.80		71.35	
K (%)	0.63		0.65		0.66	
Classes	M7		M8		M9	
	UA <sub>c</sub> (%)	PA <sub>c</sub> (%)	UA <sub>c</sub> (%)	PA <sub>c</sub> (%)	UA <sub>c</sub> (%)	PA <sub>c</sub> (%)
AG	86.41	83.09	89.00	77.93	91.00	87.53
WT	82.18	76.36	83.81	82.14	89.00	87.20
GL	80.37	89.47	83.33	90.92	88.68	92.89
WA	97.00	61.68	99.02	87.09	97.03	87.10
NF	88.07	97.43	88.18	97.84	88.99	97.63
PF	95.96	80.74	93.00	75.62	94.95	81.78
UA	95.28	73.16	100.00	86.97	92.73	87.44
OA (%)	85.56		87.44		90.29	
K (%)	0.82		0.84		0.88	

The description of the land cover classes is given in Table 3, and the description of acronyms and data input models are found in Table 4.

## References

1. Avatar, R.; Takeuchi, W.; Sawada, H. Full polarimetric PALSAR-based land cover monitoring in Cambodia for implementation of REDD policies. *Int. J. Digit. Earth*. **2013**, *6*, 255–275. [\[CrossRef\]](#)
2. Furtado, L.F.A.; Silva, T.S.F.; Fernandes, P.J.F.; Novo, E.M.L.M. Land cover classification of Lago Grande de Curuai floodplain (Amazon, Brazil) using multi-sensor and image fusion techniques. *Acta Amaz.* **2015**, *25*, 195–202. [\[CrossRef\]](#)
3. Pavanelli, J.A.P.; Santos, J.R.; Galvão, L.S.; Xaud, M.; Xaud, H.A.M. PALSAR-2/ALOS-2 and OLI/LANDSAT-8 data integration for land use and land cover mapping in northern Brazilian Amazon. *Bol. Ciênc. Geod.* **2018**, *24*, 250–269. [\[CrossRef\]](#)
4. Souza Mendes, F.; Baron, D.; Gerold, G.; Liesenberg, V.; Erasmi, S. Optical and SAR Remote Sensing Synergism for Mapping Vegetation Types in the Endangered Cerrado/Amazon Ecotone of Nova Mutum—Mato Grosso. *Remote Sens.* **2019**, *11*, 1161. [\[CrossRef\]](#)
5. Bamler, R. Principles of synthetic aperture radar. *Surv. Geophys.* **2000**, *21*, 147–157. [\[CrossRef\]](#)
6. Chen, K.-S. *Principles of Synthetic Aperture Radar Imaging: A System Simulation Approach*; CRC Press: Boca Raton, FL, USA, 2016; p. 236.
7. Bovenga, F. Special Issue Synthetic Aperture Radar (SAR) Techniques and Applications. *Sensors* **2020**, *20*, 1851. [\[CrossRef\]](#)
8. Furtado, L.F.A.; Silva, T.S.F.; Novo, E.M.L.M. Dual-season and full-polarimetric C band SAR assessment for vegetation mapping in the Amazon várzea wetlands. *Remote Sens. Environ.* **2016**, *174*, 212–222. [\[CrossRef\]](#)

9. Varghese, A.O.; Suryavanshi, A.; Joshi, A.K. Analysis of different polarimetric target decomposition methods in forest density classification using C band SAR data. *Int. J. Remote Sens.* **2016**, *37*, 694–709. [[CrossRef](#)]
10. Camargo, F.F.; Sano, E.E.; Almeida, C.M.; Mura, J.C.; Almeida, T. A Comparative Assessment of Machine-Learning Techniques for Land Use and Land Cover Classification of the Brazilian Tropical Savanna Using ALOS-2/PALSAR-2 Polarimetric Images. *Remote Sens.* **2019**, *11*, 1600. [[CrossRef](#)]
11. Wiederkehr, N.C.; Gama, F.F.; Mura, J.C.; Santos, J.R.; Bispo, P.C.; Sano, E.E. Analysis of the target decomposition technique attributes and polarimetric ratios to discriminate land use and land cover classes of the Tapajós region. *Bol. Ciênc. Geod.* **2019**, *25*, e2019002. [[CrossRef](#)]
12. Parida, B.R.; Mandal, S.P. Polarimetric decomposition methods for LULC mapping using ALOS L-band PolSAR data in Western parts of Mizoram, Northeast India. *SN Appl. Sci.* **2020**, *2*, 1049. [[CrossRef](#)]
13. Cassol, H.L.G.; Carreiras, J.M.B.; Moraes, E.C.; Aragão, L.E.O.C.; Silva, C.V.J.; Quegan, S.; Shimabukuro, Y.E. Retrieving Secondary Forest Aboveground Biomass from Polarimetric ALOS-2 PALSAR-2 Data in the Brazilian Amazon. *Remote Sens.* **2019**, *11*, 59. [[CrossRef](#)]
14. De Freitas, D.M.; Sano, E.E.; DE Souza, R.A. Potential of multipolarized ALOS/PALSAR satellite images to discriminate vegetation coverage in the Pantanal biome: A case study in the region of Medio Taquari, MS. *RBC* **2014**, *66*, 209–221.
15. Wiederkehr, N.C.; Gama, F.F.; Castro, P.B.N.; Bispo, P.C.; Balzter, H.; Sano, E.E.; Liesenberg, V.; Santos, J.R.; Mura, J.C. Discriminating Forest Successional Stages, Forest Degradation, and Land Use in Central Amazon Using ALOS/PALSAR-2 Full-Polarimetric Data. *Remote Sens.* **2020**, *12*, 3512. [[CrossRef](#)]
16. Moran, M.S.; Hymer, D.C.; Qi, J.; Kerr, Y. Comparison of ERS-2 SAR and Landsat TM imagery for monitoring agricultural crop and soil conditions. *Remote Sens. Environ.* **2002**, *79*, 243–252. [[CrossRef](#)]
17. Chaves, J.M.; Sano, E.E.; Guimarães, E.M.; Silva, A.S.; Meneses, P.R. Sinergismo entre dados ópticos e de radar para o estudo geológico na região de Bezerra-Cabeceiras, Goiás. *RBG* **2003**, *33*, 137–146. [[CrossRef](#)]
18. Sano, E.; Santos, E.M.; Meneses, P.R. Análise de imagens do satélite ALOS PALSAR para o mapeamento de uso e cobertura da terra do Distrito Federal. *Geociências* **2009**, *28*, 441–451.
19. Huang, S.; Potter, C.; Crabtree, R.L.; Hager, S.; Gross, P. Fusing optical and radar data to estimate sagebrush, herbaceous, and bare ground cover in Yellowstone. *Remote Sens. Environ.* **2010**, *114*, 251–264. [[CrossRef](#)]
20. Pereira, L.D.O.; Freitas, C.C.; Sant’Anna, S.J.S.; Lu, D.; Moran, E.F. Optical and radar data integration for land use and land cover mapping in the Brazilian Amazon. *GISci. Remote Sens.* **2013**, *50*, 301–321. [[CrossRef](#)]
21. Liesenberg, V.; de Filho, C.R.; Gloaguen, R. Evaluating moisture and geometry effects on L-Band SAR classification performance over a tropical rain forest environment. *IEEE Trans. Geosci. Remote Sens.* **2016**, *9*, 5357–5368. [[CrossRef](#)]
22. De Magalhães, T.L.; Schimalski, M.B.; Mantovani, A.; Bortoluzzi, R.L.C. Image classification using Landsat TM images to mapping wetlands vegetation (banhados) of the Catarinense Plateau, Southern Brazil. In Proceedings of the 4th GEOBIA, Rio de Janeiro, Brazil, 7–9 May 2012.
23. Polêse, C.; Oliveira, F.H.; Lima, C.L.; Alves, F.E. Análise da hidrografia da Coxilha Rica, Sul do município de Lages–SC Introdução. *Geosul* **2015**, *30*, 47–66. [[CrossRef](#)]
24. Alvares, C.A.; Stape, J.L.; Sentelhas, P.C.; De Moraes Gonçalves, J.L.; Sparovek, G. Köppen’s climate classification map for Brazil. *Meteorol. Z.* **2013**, *22*, 711–728. [[CrossRef](#)]
25. IBGE. *Mapa de Vegetação do Brasil*, 3rd ed.; Instituto Brasileiro de Geografia e Estatística: Rio de Janeiro, Brazil, 1993. Available online: [ftp://ftp.ibge.gov.br/Cartas\\_e\\_Mapas/Mapas\\_Murais/](ftp://ftp.ibge.gov.br/Cartas_e_Mapas/Mapas_Murais/) (accessed on 3 March 2020).
26. ANA-Agência Nacional De Águas. HidroWeb: Sistema de Informações Hidrológicas. Available online: <http://hidroweb.ana.gov.br> (accessed on 5 March 2020).
27. Freeman, A.; Durden, S.L. A Three-component scattering model for polarimetric SAR data. *IEEE Trans. Geosci. Remote Sens.* **1998**, *36*, 963–973. [[CrossRef](#)]
28. Cloude, S.R. Group theory and polarisation algebra. *Optik* **1986**, *75*, 26–36.
29. Lee, J.-S.; Pottier, E. *Polarimetric Radar Imaging from Basics to Applications*; CRC Press: Boca Raton, FL, USA, 2009; p. 438.
30. Qiu, F.; Berglund, J.; Jensen, J.R.; Thakkar, P.; Ren, D. Speckle Noise Reduction in SAR Imagery Using a Local Adaptive Median Filter. *GISci. Remote Sens.* **2004**, *41*, 244–266. [[CrossRef](#)]
31. Mishra, V.N.; Prasad, R.; Kumar, P.; Gupta, D.K.; Srivastava, P.K. Dual-polarimetric C-band SAR data for land use/land cover classification by incorporating textural information. *Environ. Earth Sci.* **2017**, *76*, 26. [[CrossRef](#)]
32. ESA. PolSARpro v6.0 (Biomass Edition) Toolbox. Available online: <https://step.esa.int/main/toolboxes/polsarpro-v6-0-biomass-edition-toolbox/> (accessed on 26 July 2020).
33. Meneses, P.R.; Almeida, T.D. *Introdução ao Processamento de Imagens de Sensoriamento Remoto*; UNB: Brasília, Brasil, 2012; p. 266.
34. Müller-Wilm, U.; Devignot, O.; Pessiot, L. Sen2Cor Configuration and User Manual-S2-PDGS-MPC-L2A-SUM-V2.4. Available online: [https://step.esa.int/thirdparties/sen2cor/2.4.0/Sen2Cor\\_240\\_Documentation\\_PDF/S2-PDGS-MPC-L2A-SUM-V2.4.0.pdf](https://step.esa.int/thirdparties/sen2cor/2.4.0/Sen2Cor_240_Documentation_PDF/S2-PDGS-MPC-L2A-SUM-V2.4.0.pdf) (accessed on 11 April 2020).
35. Rstudio Team. RStudio: Integrated Development for R. RStudio. Available online: <http://www.rstudio.com/> (accessed on 7 April 2020).
36. Henderson, F.M.; Lewis, A.J. *Principles and Applications of Imaging Radar*, 3rd ed.; Wiley: Hoboken, NJ, USA, 1998; p. 896.

37. Shimada, M.; Isoguchi, O.; Tadono, T.; Isono, K. Pulsar radiometric and geometric calibration. *IEEE Trans. Geosci. Remote Sens.* **2009**, *47*, 3915–3932. [[CrossRef](#)]
38. Saatchi, S.S.; Dubayah, R.; Clark, D.; Chazdon, R.; Hollinger, D. Estimation of forest biomass change from fusion of radar and lidar measurements. Available online: <http://www.slideshare.net/grssiieee/estimation-offorest-biomass> (accessed on 7 April 2020).
39. Mitchard, E.T.A.; Saatchi, S.S.; White, L.J.T.; Abernethy, K.A.; Jeffery, K.J.; Lewis, S.L.; Collins, M.; Lefsky, M.A.; Leal, M.E.; Woodhouse, I.H. Mapping tropical forest biomass with radar and spaceborne LiDAR in Lopé National Park, Gabon: Overcoming problems of high biomass and persistent cloud. *Biogeosciences* **2012**, *9*, 179–191. [[CrossRef](#)]
40. Cloude, S.R.; Pottier, E. An entropy based classification scheme for land applications of polarimetric SAR. *IEEE Trans. Geosci. Remote Sens.* **1997**, *35*, 68–78. [[CrossRef](#)]
41. Touzi, R. Target scattering decomposition in terms of roll-invariant target parameters. *IEEE Trans. Geosci. Remote Sens.* **2007**, *45*, 73–84. [[CrossRef](#)]
42. Attarchi, S.; Gloaguen, R. Classifying Complex Mountainous Forests with L-Band SAR and Landsat Data Integration: A Comparison among Different Machine Learning Methods in the Hyrcanian Forest. *Remote Sens.* **2014**, *6*, 3624–3647. [[CrossRef](#)]
43. Üstüner, M.; Gökdağ, Ü.; Bilgin, G.; Şanlı, F.B. Comparing the classification performances of supervised classifiers with balanced and imbalanced SAR data sets. In Proceedings of the Signal Processing and Communications Applications Conference (SIU), Izmir, Turkey, 2–5 May 2018; IEEE: Piscataway, NJ, USA, 2018.
44. Vapnik, V.N. *Statistical Learning Theory*; Wiley: Hoboken, NJ, USA, 1998; p. 768.
45. Li, W.; Du, Q. Support vector machine with adaptive composite kernel for hyperspectral image classification. In *Satellite Data Compression, Communications, and Processing XI*; International Society for Optics and Photonics: Baltimore, MD, USA, 2015.
46. Van der Linden, S.; Rabe, A.; Held, M.; Jakimow, B.; Leitão, P.J.; Okujeni, A.; Schwieder, M.; Suess, S.; Hostert, P. The EnMAP-Box—A Toolbox and Application Programming Interface for EnMAP Data Processing. *Remote Sens.* **2015**, *7*, 11249–11266. [[CrossRef](#)]
47. Olofsson, P.; Foody, G.M.; Stehman, S.V.; Woodcock, C.E. Making better use of accuracy data in land change studies: Estimating accuracy and area and quantifying uncertainty using stratified estimation. *Remote Sens. Environ.* **2014**, *129*, 122–131. [[CrossRef](#)]
48. Olofsson, P.; Foody, G.M.; Herold, M.; Stehman, S.V.; Woodcock, C.E.; Wulder, M.A. Good practices for estimating area and assessing accuracy of land change. *Remote Sens. Environ.* **2014**, *148*, 42–57. [[CrossRef](#)]
49. Herold, M.; Gardner, M.E.; Roberts, D.A. Spectral resolution requirements for mapping urban areas. *IEEE Trans. Geosci. Remote Sens.* **2003**, *41*, 1907–1919. [[CrossRef](#)]
50. Radoux, J.; Chomé, G.; Jacques, D.C.; Waldner, F.; Bellemans, N.; Matton, N.; Lamarche, C.; D’Andrimont, R.; Defourny, P. Sentinel-2’s Potential for Sub-Pixel Landscape Feature Detection. *Remote Sens.* **2016**, *8*, 488. [[CrossRef](#)]
51. Sothe, C.; Almeida, C.M.; Liesenberg, V.; Schimalski, M.B. Evaluating Sentinel-2 and Landsat-8 Data to Map Successional Forest Stages in a Subtropical Forest in Southern Brazil. *Remote Sens.* **2017**, *9*, 838. [[CrossRef](#)]
52. Prieto-Amparan, J.A.; Villarreal-Guerrero, F.; Martinez-Salvador, M.; Manjarrez-Domínguez, C.; Santellano-Estrada, E.; Pinedo-Alvarez, A. Atmospheric and Radiometric Correction Algorithms for the Multitemporal Assessment of Grasslands Productivity. *Remote Sens.* **2018**, *10*, 219. [[CrossRef](#)]
53. Ettehadi Osgouei, P.; Kaya, S.; Sertel, E.; Alganci, U. Separating Built-Up Areas from Bare Land in Mediterranean Cities Using Sentinel-2A Imagery. *Remote Sens.* **2019**, *11*, 345. [[CrossRef](#)]
54. Kuplich, T.M. Estudos florestais com imagens de radar. *Espaç. Geogr.* **2003**, *6*, 65–90.
55. Kasischke, E.S.; Bourgeau-Chavez, L.L. Monitoring South Florida wetlands using ERS-1 SAR imagery. *Photogramm Eng. Remote Sens.* **1997**, *63*, 281–291.
56. Leckie, D.G.; Ranson, K.J. Forest applications using imaging radar. In *Principles and Applications of Imaging Radar*, 3rd ed.; Henderson, F.M., Lewis, A.J., Eds.; Wiley: Hoboken, NJ, USA, 1998; Volume 2, pp. 435–509.
57. Formaggio, A.R.; Epiphanyo, J.C.N.; Simões, M.D.S. Radarsat backscattering from an agricultural scene. *Pesq. Agropec. Bras.* **2001**, *36*, 823–830. [[CrossRef](#)]
58. Oliver, C.J.; Quegan, S. *Understanding Synthetic Aperture Radar Images*; Scitech Publishing: Raleigh, NC, USA, 2004; p. 512.
59. Martins, F.D.; Santos, J.R.; Galvão, L.S.; Xaud, H.A. Sensitivity of ALOS/PALSAR imagery to forest degradation by fire in northern Amazon. *Int. J. Appl. Earth Obs. Geoinf.* **2016**, *49*, 49–163. [[CrossRef](#)]
60. Cloude, S.R.; Pottier, E. A review of target decomposition theorems in Radar Polarimetry. *IEEE Trans. Geosci. Remote Sens.* **1996**, *34*, 498–518. [[CrossRef](#)]
61. Zou, T.; Yang, W.; Dai, D.; Sun, H. Polarimetric SAR image classification using multifeatures combination and combination and extremely randomized clustering forests. *EURASIP J. Adv. Signal Process.* **2009**, *2010*, 465612. [[CrossRef](#)]
62. Longepe, N.; Rakwatin, P.; Isoguchi, M.; Shimada, M.; Uryu, Y.; Yulianto, K. Assessment of ALOS PALSAR 50 m orthorectified FBD data for regional land cover classification by support vector machines. *IEEE Trans. Geosci. Remote Sens.* **2011**, *262*, 1786–1798. [[CrossRef](#)]
63. Attarchi, S. Extracting impervious surfaces from full polarimetric SAR images in different urban areas. *Int. J. Remote Sens.* **2020**, *41*, 4644–4663. [[CrossRef](#)]
64. Guimarães, U.S.; Galo, M.L.B.T.; Narvaes, I.S.; Silva, A.Q. Cosmo-SkyMed and TerraSAR-X datasets for geomorphological mapping in the eastern of Marajó Island, Amazon coast. *Geomorphology* **2020**, *350*, 106934. [[CrossRef](#)]

65. Pulella, A.; Aragão Santos, R.; Sica, F.; Posovszky, P.; Rizzoli, P. Multi-Temporal Sentinel-1 Backscatter and Coherence for Rainforest Mapping. *Remote Sens.* **2020**, *12*, 847. [[CrossRef](#)]
66. Voormansik, K.; Zalite, K.; Sünter, I.; Tamm, T.; Koppel, K.; Verro, T.; Brauns, A.; Jakovels, D.; Praks, J. Separability of Mowing and Ploughing Events on Short Temporal Baseline Sentinel-1 Coherence Time Series. *Remote Sens.* **2020**, *12*, 3784. [[CrossRef](#)]
67. Almeida, J.A.; Albuquerque, J.A.; Bortoluzzi, R.L.C.; Mantovani, A. Caracterização dos solos e da vegetação de áreas palustres (brejos e banhados) do Planalto Catarinense. Available online: [http://solos-sc.com.br/index.php/conteudo/file/174-relatorio%20final\\_caracterizacao%20dos%20solos%20e%20da%20vegetacao%20de%20areas%20palustres-brejos%20e%20banhados-%20do%20planalto%20catarinense](http://solos-sc.com.br/index.php/conteudo/file/174-relatorio%20final_caracterizacao%20dos%20solos%20e%20da%20vegetacao%20de%20areas%20palustres-brejos%20e%20banhados-%20do%20planalto%20catarinense) (accessed on 7 April 2020). (In Portuguese).
68. Pal, M.; Foody, G.M. Feature selection for classification of hyperspectral data by SVM. *IEEE Trans. Geosci. Remote Sens.* **2010**, *48*, 2297–2307. [[CrossRef](#)]
69. Rabe, A.; Van Der Linden, S.; Hostert, P. Simplifying support vector machines for classification of hyperspectral imagery and selection of relevant features. In Proceedings of the 2nd Workshop on Hyperspectral Image and Signal Processing: Evolution in Remote Sensing, Reykjavik, Iceland, 14–16 June 2010; IEEE: Piscataway, NJ, USA, 2010.
70. Waske, B.; Van Der Linden, S.; Benediktsson, J.A.; Rabe, A.; Hostert, P. Sensitivity of support vector machines to random feature selection in classification of hyperspectral data. *IEEE Trans. Geosci. Remote Sens.* **2010**, *48*, 2880–2889. [[CrossRef](#)]
71. van Beijma, S.; Chatterton, J.; Page, S.; Rawlings, C.; Tiffin, R.; King, H. The challenges of using satellite data sets to assess historical land use change and associated greenhouse gas emissions: A case study of three Indonesian provinces. *Carbon Manag.* **2018**, *9*, 399–413. [[CrossRef](#)]